

ORIGINAL RESEARCH ARTICLE

Archimetrics: a quantitative tool to predict three-dimensional meander belt sandbody heterogeneity

WIETSE I. VAN DE LAGEWEG*, WOUT M. VAN DIJK†, DARREN BOX‡ and MAARTEN G. KLEINHANS*

*Faculty of Geosciences, Universiteit Utrecht, P.O. Box 80115, 3508 TC, Utrecht, The Netherlands

†Department of Geography, Durham University, South Road, Durham, DH1 3LE, UK

‡ExxonMobil Russia, 31 Novinsky Boulevard, 123242, Moscow, Russia (Email: wietse.vandelageweg@gmail.com)

Keywords

Flume experiment, fluvial architecture, meander belt, meandering river, morphodynamic modelling, preservation, sandbody heterogeneity, stratigraphy.

Manuscript received: 4 December 2015;

Accepted: 14 March 2016

The Depositional Record 2016; 2(1): 22–46

doi: 10.1002/dep.2.12

ABSTRACT

Fluvial meander belt sediments form some of the most architecturally complex reservoirs in hydrocarbon fields due to multiple scales of heterogeneity inherent in their deposition. Currently, characterization of meander belt bodies largely relies on idealized vertical profiles and a limited number of analogue models that naively infer architecture from active river dimensions. Three-dimensional architectural data are needed to quantify scales of grain-size heterogeneity, spatial patterns of sedimentation and bar preservation in a direct relationship with the relevant length scales of active river channels. In this study, three large flume experiments and a numerical model were used to characterize and construct the architecture (referred to as ‘archimetrics’) and sedimentology of meander belt deposits, while taking reworking and partial preservation into account. Meander belt sandbody width-to-thickness ratios between 100 and 200 were observed, which are consistent with reported values of natural meander belts. For the first time, the relief of the base of a meander belt is quantified, enabling improved estimates of connectedness of amalgamated meander belts. A key observation is that the slope and number of lateral-accretion packages within natural point bar deposits can be well predicted from fairly basic observables, a finding subsequently tested on several natural systems. Probability curves of preserved architectural characteristics for three dimensions were quantified allowing estimates of bar dimensions, baffle and barrier spacing distributions and container dimensions. Based on this, a set of rules were identified for combining reservoir parameters with the identified probability curves on sandbody dimensions and character, to help create more realistic geomodels for estimating exploration success on the basis of seismic and core data.

INTRODUCTION

Characterization and prediction of the three-dimensional architecture and fluid-flow behaviour of fluvial hydrocarbon reservoirs and drinking water aquifers is challenging because of the various scales of sediment heterogeneity between and within fluvial deposits (Miall, 1988; Jordan & Pryor, 1992; Pranter *et al.*, 2007; Willis & Tang, 2010). In essence, fluvial deposits are composed of a number of architectural elements (Miall, 1985; Holbrook, 2001) spanning a wide range of spatial and temporal scales (Fig. 1). The heterogeneity of fluvial deposits at the scale of a hydrocarbon field (i.e. heterogeneity levels

1 and 2 of Jordan & Pryor, 1992) primarily depends on channel belt sandbody (i.e. Fig. 1, sixth-order contacts) stacking patterns and the associated connectivity between individual channel belt sand bodies (Allen, 1978; Leeder, 1978; Bridge & Leeder, 1979; Mackey & Bridge, 1995). Heterogeneity within individual channel belt sand bodies also impacts performance and efficiency of reservoirs due to an internal architecture with a complex arrangement of contact surfaces, where contrasting grain size, sorting and other lithologic characteristics make for baffles and barriers to flow (Tyler & Finley, 1991; Pranter *et al.*, 2007; Donselaar & Overeem, 2008; Willis & Tang, 2010).

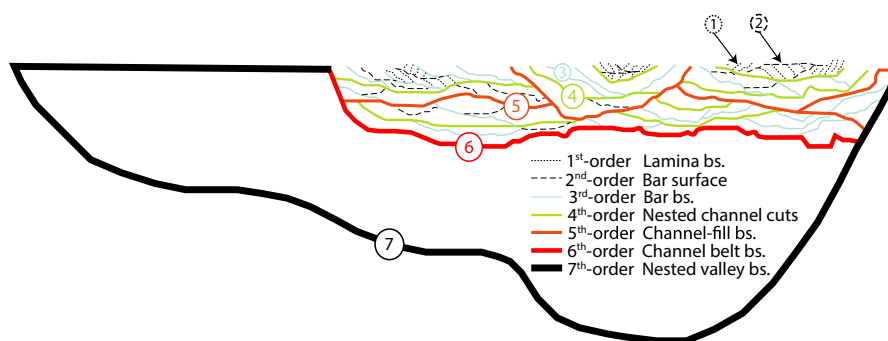


Fig. 1. The hierarchy of fluvial architectural elements. In this study, the focus is on third-order to sixth-order bounding contacts: bar boundaries, nested channel cuts, channel fill and lateral-accretion element boundaries and the external geometry of meander belt sand bodies. Modified from Miall (1985), Holbrook (2001) and Van de Lageweg *et al.* (2015).

Efforts to quantify fluvial meander belt architecture until now focused on vertical core data (Paola & Borgman, 1991), ignoring the horizontal dimensions. In practice this has the consequence that three-dimensional geomodels developed for flow calculations (i.e. heterogeneity levels 1 and 2 of Jordan & Pryor, 1992) have had to assume either geostatistical or geometrical body dimensions derived from natural rivers (Pranter *et al.*, 2007). However, this approach largely neglects internal heterogeneity and the highly fragmented nature of fluvial three-dimensional bodies (Parker *et al.*, 2013; Van de Lageweg *et al.*, 2013a,b). At the other end of the hierarchical spectrum, quantitative descriptions of preserved laminae, ripples and dunes (Bridge & Best, 1997; Storms *et al.*, 1999; Leclair, 2002) could be used to populate low-order (i.e. Fig. 1, first-order to third-order) architectural bodies. However, populating flow models based on individual order statistics would largely ignore the inherent hierarchical relationships and connectivity between the different architectural levels of fluvial deposits.

Reservoir geocellular modelling requires quantitative information on the geometries and material properties of reservoir bodies at all hierarchical levels (Fig. 1) to build realistic geological models with predictive flow simulation. However, the large-scale sandbody architecture and stratigraphic and sedimentary heterogeneity within channel belt sand bodies is commonly difficult to model from subsurface data with a typical well spacing between 200 m and 400 m in developed fields (Pranter *et al.*, 2007). This generally results in a lack of architecturally detailed deterministic information. As a consequence, geomodellers often turn to modern analogues (Yang & Sun, 1988; Bhattacharya & Tye, 2004) or outcrops (White & Barton, 1999; Willis & White, 2000) in an effort to obtain quantitative stratigraphic information required to accurately populate the geological model.

The dimensions and distributions of sand bodies and shales are critical parameters in designing a meaningful reservoir model. Sand bodies are generally described by width-to-thickness ratio, net-to-gross (sandstone to shale) ratio, and connectedness ratio (Gibling, 2006; Gouw & Autin, 2008). Point bar deposits are among the largest and architecturally most complex reservoir bodies formed by fluvial meandering systems. In particular, point bar lateral-accretion elements and the associated shale that drape them are potential baffles and barriers to fluid flow and may therefore act to compartmentalize reservoirs (Willis & White, 2000; Pranter *et al.*, 2007; Donselaar & Overeem, 2008; Willis & Tang, 2010). In addition, internal facies trends, for example, the commonly described vertical change from cross-bedded coarse and medium-grained sands to silt laminated ripples in point bar deposits (Nanson, 1980; Bridge *et al.*, 1995), generate a fining-upward succession that potentially can affect the porosity and permeability of reservoirs and bodies.

To improve our ability to build geologically sound models of reservoirs formed by fluvial meandering systems, we must improve our ability to predict the external geometry of meander belt sand bodies, their internal architecture, composed of channel fills and point bar deposits, and the distribution, thickness and orientation of muds. In addition, an explicit link between the causal process of river meandering and the resultant architecture will help elucidate the effect that changing discharge, channel depth and sediment has on the formation and preservation of meander belt deposits, allowing for a better understanding and predictive ability of spatial patterns in sedimentation and preservation. Here, the dimensionless size ratios between the formative meandering channel (i.e. depth, width and meander length of the channel) and the resultant architectural elements (i.e. thickness, width and length of point bar deposits) are developed to make comparisons between systems of

different size possible. These dimensionless size ratios between morphological form and depositional product are referred to as archimetrics, inspired by empirical morphometric relationships derived from modern meandering rivers (Leopold & Wolman, 1957; Zeller, 1967; Kleinhans & Van den Berg, 2011). The idea behind the analysis is that we use known morphodynamic relationships as the relevant length scales for the resulting deposits, while incorporating reworking and partial preservation statistics.

The objective of this study is therefore to develop quantitative three-dimensional relationships that describe the stratigraphical and sedimentological architecture of meandering rivers. This depositional model should aid architectural characterization and geomodel building for fluid-flow calculations in the hydrocarbon development and production phases of reservoirs composed of meander belt deposits. Deposits formed by meandering rivers are emphasized because of their considerable lithological variation and because their reservoir behaviour has proven challenging to predict to date (Willis & White, 2000; Pranter *et al.*, 2007; Donselaar & Overeem, 2008; Willis & Tang, 2010). The depositional model is developed using three flume experiments and one numerical model. The specific objectives of this study are to:

- 1 Quantify the external geometry of meander belts: width, thickness and the relief variation of the base of meander belts.
- 2 Quantify the three-dimensional internal stratigraphic architecture of meander belts using internal bounding surfaces that are formed by channel migration and bend cut-off.
- 3 Quantify relationships between dimensions of non-truncated morphological elements (e.g. channel depth and meander length) and dimensions of truncated, partially preserved architectural elements.
- 4 Evaluate the processes that control the distribution and dimension of fines within point bar deposits, in particular lateral-accretion surfaces.
- 5 Compare observed lateral slopes of accretion surfaces to predictions by a semi-empirical relationship that predicts these surfaces as a function of observable channel and sediment characteristics.
- 6 Identify a set of rules for building realistic three-dimensional reservoir models of deposits formed by meandering rivers.

DATA AND METHODOLOGY

Three flume experiments and one numerical model simulation were used in this study. The complementary nature of models and experiments and the benefits of using both have been discussed elsewhere (Kleinhans *et al.*, 2014). Experiment A and the numerical model focused on the

formation of channel bounding surfaces. The dimensionless archimetric size ratios from experiment A were quantitatively compared to the numerical model to evaluate possible scale dependence and effects of different styles of bend cut-off. By including flume experiments as well as a numerical model it is intended to move beyond effects of initial setups and specific boundary conditions. When commonalities in, for example, the meander belt width-to-thickness ratios arise for two completely different approaches and scales, it is likely that they are not related to initial and boundary conditions and therefore have a wider validity. Experiments B and C focused on the deposition of fine sediment in point bar deposits, which cannot presently be modelled yet with the detail that experiments deliver.

First, the setups and procedures of experiments A, B and C are described. Second, the numerical model settings are given. Third, the data processing work flow for the flume experiments and the numerical model are explained.

Experimental setups

Experiments A and B have been published elsewhere (Van Dijk *et al.*, 2012, 2013b; Van de Lageweg *et al.*, 2013a,b, 2014) while the present analyses and Experiment C are novel. All experiments were conducted in a flume 6 m wide and 10 m long. The design conditions were not derived from direct scaling of a specific river but are based on a minimization of scaling issues, that is, low sediment mobility, scour hole formation and sediment cohesion (see full review in Kleinhans *et al.*, 2010, 2014). Key dimensionless variables were therefore kept within a range of values to ensure process similarity with natural meandering coarse-grained rivers. For flow similarity, Froude numbers (Fr) must be subcritical ($Fr < 1$) and flow must be turbulent ($Re > 2000$). Rough flow conditions were ascertained by the use of a poorly sorted sand (D_{10} , D_{50} and D_{90} are 0.25, 0.51 and 1.35 mm, respectively). Furthermore, the upstream water and sediment supply point was dynamic and moved transversally in both directions. Pilot experiments (not reported here) showed that meander dynamics were not sustained in the absence of this upstream perturbation. In agreement with (Lanzoni & Seminara, 2006), Van Dijk *et al.* (2012) showed that the direct effect of the transversal perturbation on downstream bend development was limited to the development of the first bend; yet the presence of the perturbation ensured dynamic meandering with repeated chute cut-offs. Based on observed bend migration rates during the pilot experiments, a constant rate of movement of 1 cm/hour was applied for all flume experiments.

The general settings of experiments A, B and C were similar but a number of specific conditions differed (Table 1). Experiment A had an initial straight channel that was 0.3 m wide, 0.015 m deep and set at a gradient of 0.0055 m/m. Sediment and water were supplied at constant rates of 0.75 l/hr and 1 l/s, respectively. The sediment feed consisted of a mixture of poorly sorted sand and 20 volume per cent of silt-sized silica flour (D_{10} , D_{50} and D_{90} are 3.7 μm , 32 μm and 97 μm , respectively). The silt-sized silica flour formed weakly cohesive deposits and limited channel widening, which would otherwise ultimately have resulted in a braided channel pattern (Peakall *et al.*, 2007; Van Dijk *et al.*, 2012). The duration of experiment A was 260 hours.

Experiment B (Van Dijk *et al.*, 2013b; Van de Lageweg *et al.*, 2014) had an initial straight channel that was 0.15 m wide, 0.01 m deep and set at a gradient of 0.01 m/m (Table 1). A simple stepped shape hydrograph was used with a long (2.5 hours) duration low discharge of 0.25 l/s and a short (0.5 hours) duration high discharge of 0.5 l/s. The stepped shape hydrograph was not intended to represent the flood hydrograph of a specific river but was introduced to stimulate overbank flow and overbank deposition of fines. To this end, an additional 0.5 l of silt-sized silica flour was added during the high discharge stages of the hydrograph. The low discharge sediment feed rate was 0.2 l/hr. This sediment feed had an identical composition for flume experiments A and B. The duration of experiment B was 120 hours.

The design conditions of experiment C were identical to those of experiment B (Table 1). The only difference was that experiment C used walnut shell fragments instead of silt to simulate fines. The walnut shell fragments were well-sorted (between 1.3 mm and 1.7 mm) and behaved as suspended load. It is hypothesized that the silt and walnut shells may capture different depositional behaviour in natural systems. Specifically, the applied walnut shells may represent very fine, highly mobile and mostly suspended materials such as clay and fine silts, whereas the applied silts may be a proxy for coarser, less mobile and bedload to suspended load

materials such as coarse silt and fine sand. During high discharge 1 l of walnut fragments was added. The long duration (multiple weeks) of these large-scale experiments limited the applicability of walnut fragments because they started to decompose after a few weeks. A minor amount of an oily substance was released during this walnut decomposition, which caused cohesive behaviour such that the river planform ossified. We used the initial point bar deposits that were formed prior to ossification to compare the spatial distribution of walnut shells in experiment C to that of the silt in experiment B, because the two different experimental methods to simulate fine-sediment deposits gave complementary results.

Surface elevation data were collected every 8 hours for experiment A and every 3 hours for experiments B and C. A line-laser with a vertical resolution of 0.2 mm recorded the elevation of the fluvial morphology at longitudinal increments of 2 mm. The point cloud from the line-laser was median filtered on to a 10-mm grid for experiment A and on to a 4-mm grid for experiments B and C to produce Digital Elevation Models (DEMs). See Van Dijk *et al.* (2012) and Van de Lageweg *et al.* (2013a) for a more detailed description of data reduction from the line laser.

In addition, a high-resolution (0.25 mm ground resolution) camera photographed the fluvial surface in experiments B and C. In experiment B, these high-resolution images were used to derive silt surface concentrations (see also Van Dijk *et al.*, 2013b). The high-resolution camera with RGB-band gives values for green, red and blue, which were transformed to a *LAB* colour space. In this colour space, *L* corresponds to luminosity (low = black and high = white), *A* reflects the position between red/magenta (high values) and green (low values), and *B* is the position between yellow (high values) and blue (low values). The luminosity was used here to make distribution maps of the highly reflective silt-sized silica flour (Fig. 2). For every survey, 36 individual images (Fig. 2A) were collected and tied to the DEM by the mutual robot coordinate system.

Table 1. Design conditions of flume experiments and numerical model run

Parameter Used for	Flume experiment A Bounding contacts	Flume experiments B and C Fines	Numerical model Bounding contacts
Length	10 m	10 m	10 000 m
Width	6 m	3 m	3000 m
Initial channel width	0.3 m	0.15 m	200 m
Initial channel depth	0.015 m	0.01 m	8 m
Width-to-depth ratio	20	15	25
Discharge	$1 \times 10^{-3} \text{ m}^3/\text{s}$	0.25 and $0.5 \times 10^{-3} \text{ m}^3/\text{s}$	$2500 \text{ m}^3/\text{s}$
Basin slope	5.5×10^{-3}	1×10^{-2}	2×10^{-4}

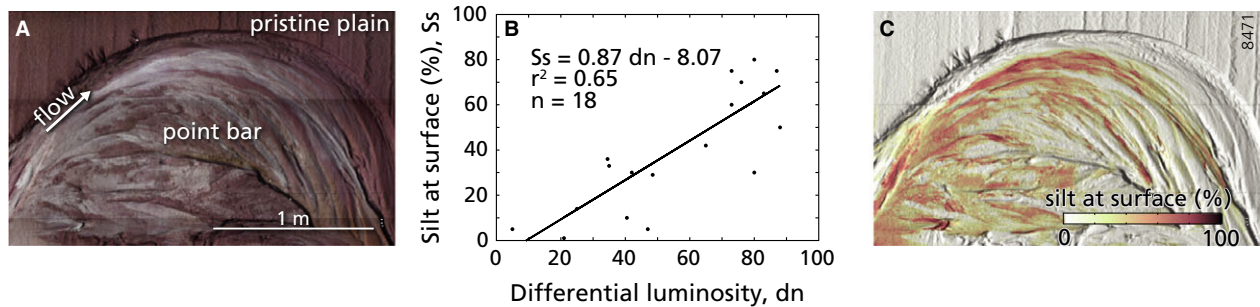


Fig. 2. Illustration of the method used to convert image whiteness to silt concentration. (A) Rectified image of experiment B with silt deposition (white) on top of point bar. (B) Least-squares linear relationship between differential luminosity (quantified by the image digital number dn) and measured silt surface concentrations (S_s). (C) Silt surface concentrations of image shown in (A). Note that the whiter areas in (A) have a higher silt surface concentration. Modified from Van de Lageweg *et al.* (2014).

Post-experiment, 18 silt samples were collected that were related to the luminosity difference between each survey image and the initial image of the bed for that location (Fig. 2B). Similar relationships were found in other tests and experiments supporting the validity of this relationship. This relationship was then used to convert the luminosity maps to silt surface distribution maps (Fig. 2C). In experiment C, the high-resolution images were used to examine the sedimentation pattern of walnut shell fragments. Experiment C served to compare the spatial distribution of walnut shells to that of silt and therefore only the last time step prior to ossification is presented.

Numerical model setup

A highly sinuous meandering river and resultant sandbody architecture was simulated by the two-dimensional fluid dynamics and morphodynamics code NAYS2D (Asahi *et al.*, 2013; Schuurman *et al.*, 2015; Van de Lageweg *et al.*, 2015). This process-based model is the first to produce river meandering without presuming a fixed relationship between bank erosion and bank accretion, contrary to one-dimensional meander simulation models (Willis & Tang, 2010). This key feature of NAYS2D to simulate inner bend bar accretion and outer bend bank erosion independently allows for channel width variations, which are known to affect hydrodynamics (Zolezzi *et al.*, 2012; Frascati & Lanzoni, 2013) and sediment deposition along meander bends (Eke *et al.*, 2014; Van de Lageweg *et al.*, 2014).

The NAYS2D model parameters were chosen such that a dynamic and sustained freely meandering river was simulated. The full model domain was 3 km wide and 10 km long. Runs started from a straight 200 m wide and 8 m deep channel set at a gradient of 2×10^{-4} m/m (Table 1). To maintain model stability, channels were not

allowed to erode beyond 8 m below the initial floodplain level although bars could freely aggrade. Sediment transport rate was computed by the Engelund & Hansen (1967) formulation. A uniform grain size of 2 mm was applied and discharge was maintained constant at $2500 \text{ m}^3/\text{s}$ following similar simplified approaches in Schuurman *et al.* (2013, 2015). In this approach, constant discharge is assumed to be the dominant or effective discharge integrating all the morphodynamic work done over a yearly hydrograph. A constant uniform bed roughness (Nikuradse $k_s = 0.15 \text{ m}$) was used to parameterize bed form roughness. Similar to the experimental setups, the upstream water and sediment inflow point moved transversely. The rate of movement was maintained constant at 0.65 m/yr and had a maximum amplitude of 300 m. A detailed analysis of the effect of upstream perturbations on the evolution and morphological characteristics of the meandering channel in NAYS2D and other numerical models is provided in and Schuurman *et al.* (2015).

The NAYS2D computational grid was initially straight and consisted of grid cells with a width and length of 20 m. During the run, bank erosion and bank accretion adjusted the bank lines. Curvilinear re-gridding was performed to keep the grid boundary fitted and to maintain the transverse grid lines perpendicular to the channel centre line. The dynamic coordinate system enabled channel migration and neck cut-offs but introduced some instability over the course of the run, which limited planform development to a maximum of 668 modelled time steps. Channel neck cut-offs were modelled as an instantaneous change in planform, which could occur at any time step when two migrating banks met. At the end of the model run, the dynamic coordinates of all recorded time steps were re-sampled to fixed Cartesian ones to generate DEM surfaces and three-dimensional virtual meander belt architectures.

Quantifying three-dimensional meander belt sandbody architecture

Sequential highly detailed DEMs of the meander morphology in the flume experiments and numerical model were used to generate three-dimensional synthetic sandbody architectures that record channel history and the formation of bounding contact surfaces (Fig. 3). The ability to track the morphological channel history while building three-dimensional synthetic meander belt architectures allowed the preserved sandbody architecture to be explicitly related to original meander morphology at the time of sedimentation. From this three-dimensional architectural output, virtual cores, transects and maps were constructed and analysed.

Meander belt sandbody architecture from the flume experiments and numerical model was analysed in three dimensions. To this end, we extracted virtual cores in all three directions through the depositional block to calculate statistics of thicknesses, widths and lengths between bounding surfaces (Fig. 4). Set thickness is defined as a depositional body enclosed by two successive bounding surfaces in a vertical direction (z), set length as a depositional body enclosed by two successive bounding surfaces in a longitudinal direction (x), and set width as a depositional body enclosed by two successive bounding surfaces in a lateral direction (y) (Fig. 4C, see also Van de Lageweg *et al.*, 2013a). The number of grid points and therefore the number of virtual cores was large with, for

example, $2 \times 3 \cdot 10^5$ vertical cores for experiment A, $1 \times 2 \cdot 10^6$ vertical cores for experiment B and $3 \times 8 \cdot 10^4$ vertical cores for the numerical model run. It is important to note that the identified surfaces and units merely served as a quantitative framework for the meander belt architecture and do not necessarily relate to lithostratigraphic sand bodies that would define reservoir heterogeneities or to specific scales of depositional bed or bedform. Although heterogeneity patterns can follow depositional bed surface geometry, this is not always the case and has also not been assessed in this study.

In order to generalize results, the extracted set thicknesses, set widths and set lengths were compared with morphometric parameters that are commonly used to describe meander morphology (Fig. 4). For this purpose, the mean channel depth (h_{mean}), mean meander bend length (L_{bend}), mean channel width (w_{mean}) and mean meander bend amplitude (A_{bend}) were used to summarize the meander morphology in the flume experiments as well as the numerical model. For simplicity and easier field application, the A_{bend} was approximated by $0.5 \times$ meander belt width. Archimetrics were then calculated as the dimensionless size ratios between the set statistics characterizing meander belt sandbody architecture and the morphological statistics characterizing the original meander form: set thickness was related to h_{mean} , set length to L_{bend} and set width to A_{bend} and w_{mean} .

The detection of bounding surfaces and contacts in flume experiment A was defined by the vertical resolution

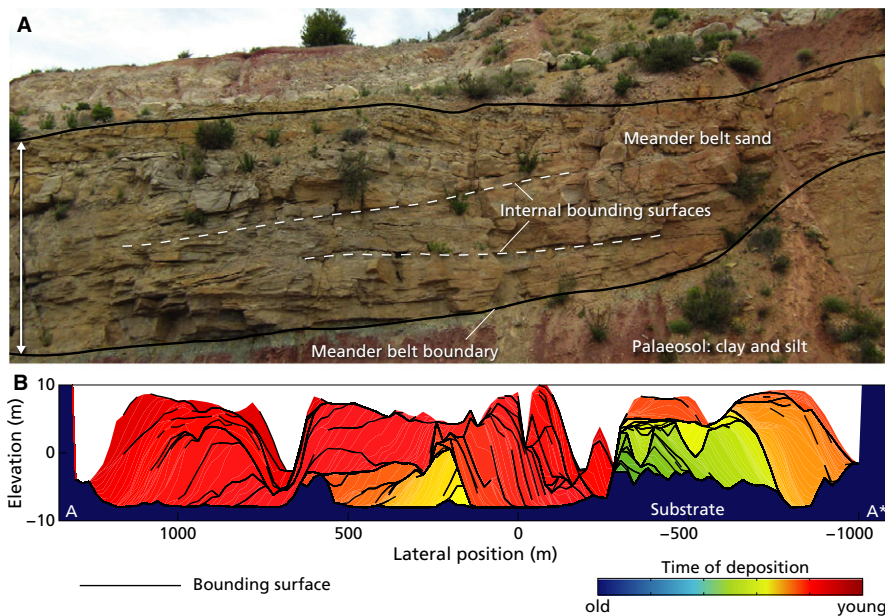


Fig. 3. Meander belt architecture formed by (A) nature and (B) the numerical model NAYS2D. The meander belt architecture resulting from the numerical model and flume experiments is referred to as 'synthetic stratigraphy' and is used to infer time of deposition, channel scour surfaces and typical thicknesses, widths and lengths between channel and scour bounding surfaces. The position of the synthetic slice A-A* is indicated in Fig. 5C.

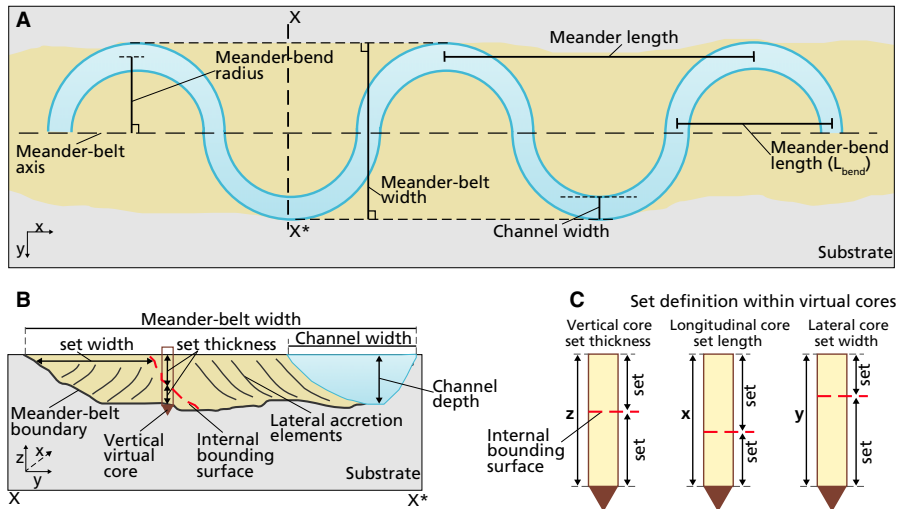


Fig. 4. Schematic drawing of morphometric and archimetric parameters used to quantify meander morphology and architecture. (A) Map view of meander belt with definition of key morphometric parameters. (B) Cross-section of meander belt with definition of key morphometric and archimetric parameters. (C) Set definition within virtual cores. Cores were made in vertical (z), longitudinal (x) and lateral (y) direction. We define set thickness as a depositional body enclosed by two successive bounding surfaces in vertical direction, set length as a depositional body enclosed by two successive bounding surfaces in longitudinal direction, and set width as a depositional body enclosed by two successive bounding surfaces in lateral direction.

of the line laser. All features smaller than 0.2 mm could not be detected and elevation differences between sequential DEMs smaller than or equal to 0.2 mm were therefore removed. In the numerical model, bounding surfaces formed by smaller scale features such as dunes and ripples were not explicitly modelled. Their height was estimated from the prescribed bed roughness as $h_{dune} = 2 \cdot k_s$ (Van Rijn, 1984). This resulted in a typical h_{dune} of 0.3 m. Bounding surfaces resulting from an erosion event with a magnitude of 0.3 m or less were removed, implicitly ensuring that the channel and bar scouring and channel cut-offs were the only formative processes feeding into the synthetic stratigraphy.

Lateral-accretion surface slopes in point bar deposits correspond to the transverse bed slopes of meander inner bends. The transverse bed slope of the meander inner bend in flume experiment B was measured and compared the slope to a transverse bed slope predictor derived from physics. The analytical prediction for the transverse bed slope ($\tan \frac{\partial z}{\partial n}$) was solved at the meander bend apex (Struiksma, 1985; Talmon *et al.*, 1995):

$$\tan \frac{\partial z}{\partial n} = 9 \cdot \left(\frac{D_{50}}{h} \right)^{0.3} \cdot \sqrt{\theta} \cdot \frac{2}{\kappa^2} \cdot \left(1 - \frac{\sqrt{g}}{\kappa \cdot C} \right) \cdot \frac{h}{R} \quad (1)$$

where h is water depth (m), g is gravitational acceleration (m^2/s), θ is Shields sediment mobility number, C is the Chézy number (here calculated as $18 \cdot \log \left(\frac{12h}{D_{90}} \right)$), κ is the Von Kármán's constant (0.4) and R is the radius of

curvature of the streamlines. This relationship has been tested successfully in experiments (Van Dijk *et al.*, 2012, 2013a) and in the field (Kleinhans *et al.*, 2012) and in many engineering applications). Following Struiksma (1985), the transverse bed slope was determined by selecting the observations at $0.1w$ (here 2 cm) from the deepest measurement on the profile and at $0.1w$ from the water line. The transverse bed slope, h was assumed constant at 0.011 m, while R changed.

RESULTS

The meander morphodynamics are initially described here and typical morphometrics for flume experiment A, flume experiment B and the numerical model are identified. Then, the dimensions of architectural elements of meander belt deposits formed in the flume experiments and the numerical model are quantified. Following earlier work on fluvial architectural elements and contact surfaces (Miall, 1985; Holbrook, 2001), a hierarchical approach is adopted to describe and quantify the architectural elements: starting with the largest element corresponding to the external geometry of meander belt sand bodies (Fig. 1, sixth-order contacts), then focusing on the internal sandbody architecture of a meander belt (Fig. 1, fifth- to third-order contacts) and finally zooming in to the point bar lateral-accretion elements (Fig. 1, third order) and associated shale drapes.

Meander morphodynamics

In flume experiment A (Fig. 5A), the initial straight channel developed into a low-sinuuous meandering river. The meandering channel was on average about 0.25 m wide and 0.015 m deep, resulting in a width-to-depth ratio of 17. Typically, L_{bend} was about 3.5 m. Point bars were the dominant morphology throughout the experiment although the initial point bar bodies became increasingly dissected as the experiment progressed.

Initially, a series of point bars raised channel sinuosity, calculated as the ratio between the length along the channel and the straight-line distance between the ends of the channel, to a maximum of about 1.3 in flume experiment A. With this higher sinuosity, water started to flow across the point bar surface and eventually a chute cut-off took place. Former active channels transformed into floodplain lakes, which remained as topographic lows in this experiment because of the limited amount of fine-grained silica flour available as fill. The floodplain depressions were thus easily re-occupied and re-activated by the channel through chute cut-offs. In total, four chute cut-offs were observed during experiment A. The morphology at the end of the experiment consisted of a large number of point bars that were mostly cross-cut by chute cut-offs. A qualitative comparison shows that this morphological configuration has similarities with the 'coarse-grained meandering stream': model 5 of Miall (1985), which agrees with the analysis presented here that the experimental meandering rivers represent gravel-bed rivers best (Kleinmans *et al.*, 2014).

In flume experiment B (Fig. 5B), the meandering river was characterized by sustained lateral migration of the channel and the absence of cut-offs in the middle section

of the flume. Channel sinuosity increased to 1.4 at the end of this experiment. Due to the lower discharge in experiment B compared to experiment A (Table 1), the channel had smaller dimensions: the channel was on average 0.2 m wide, 0.011 m deep, with a resultant width-to-depth ratio of 17, and had a typical L_{bend} of about 2.2 m.

The absence of chute cut-offs in flume experiment B was caused by the addition of more cohesive fine material to the sediment feed compared to experiment A. These cohesive fines were deposited on the floodplain when the water level exceeded bankfull conditions. Initially, this mainly occurred during the brief high-flow stages. As the experiment progressed and the meander bend sharpened, channel gradient reduced so that water levels generally increased and overbank flow also occurred during low-flow stages. Although overbank deposition of the fine silt only resulted in thin sheet splays and levees, depressions on the point bar surface could not be re-activated and chute cut-offs did not occur.

In the numerical model (Fig. 5C), the initial straight channel developed into a highly sinuous ($S \sim 1.5-2$) meandering channel. The sinuous single-thread channel was on average 8 m deep but locally reached depths of up to about 20 m, measured from the top of aggraded bars to the channel bottom. The deepest parts corresponded to outer bends while inner bends were notably shallower. Channel width also varied greatly with an average of 250 m, resulting in a typical width-to-depth ratio of 31, but locally it was only 180 m wide while the maximum observed channel width was 280 m. Meanders had a typical L_{bend} of 1000 m. The channel was locally straightened by neck cut-offs from about 350 time steps onwards. In total, we observed four neck cut-offs. Qualitatively, the channel width-to-depth ratio and channel

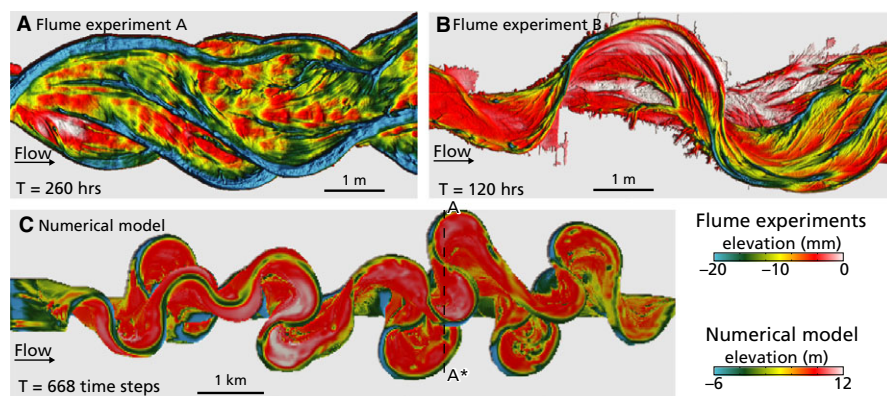


Fig. 5. Digital Elevation Models (DEMs) of meander belts that were formed in the flume experiments and numerical model. (A) DEM of flume experiment A in which a meander belt formed during constant bankfull discharge (Van de Lageweg *et al.*, 2013b; Van Dijk *et al.*, 2012). (B) DEM of flume experiment B in which a meander belt formed as the result of a variable discharge (Table 1) and addition of fine cohesive silt during the high-flow stages (Van Dijk *et al.*, 2013a; Van de Lageweg *et al.*, 2014). (C) DEM of meander belt simulated with the numerical model NAYS2D (Van de Lageweg *et al.*, 2015). Slice A-A* is presented in Fig. 3.

planform generated with the numerical model have similarities with the ‘classic meandering stream’: model 6 of Miall (1985).

Meander belt architecture

Meander belt external sandbody geometry

In the numerical model, the meander belt sandbody had an average width of 1230 m at the end of the simulation (Fig. 6A). This is equal to about $5 w_{mean}$. The meander belt sandbody had an average thickness of 8.4 m, which is in close agreement with the h_{mean} of 8 m (Fig. 6C). The relief at the base of the meander belt sandbody generally fell within h_{mean} (Fig. 6E). The base of the sandbody was deepest in the axial zone of the meander belt and persistently shallowed towards the margins of the sandbody, as evidenced by the Z_{10} distribution.

Longitudinal variations in elevation relief of the sandbody base were laterally homogeneous, as seen from the difference between the bed level Z_{10} and Z_{90} percentile profiles (Fig. 6E).

In experiment A, the meander belt sandbody had an average width of 2.1 m at the end of the experiment (Fig. 6B). This is equal to about $8 w_{mean}$. The thickness of the meander belt was on average 1.2 cm, which is close to the h_{mean} of 1.5 cm (Fig. 6D). The relief at the base of the meander belt sandbody was generally captured within h_{mean} (Fig. 6F). Re-occupation of older unfilled channels and resultant repetitive scouring and deepening of these channels led to two substantial dips in base elevation at the margins of the sandbody, most clearly seen in the Z_{10} percentile profile (Fig. 6F). Longitudinal variations in elevation relief of the sandbody base were laterally homogeneous, except for the margins of the sandbody base where a general deepening was seen on both sides of the

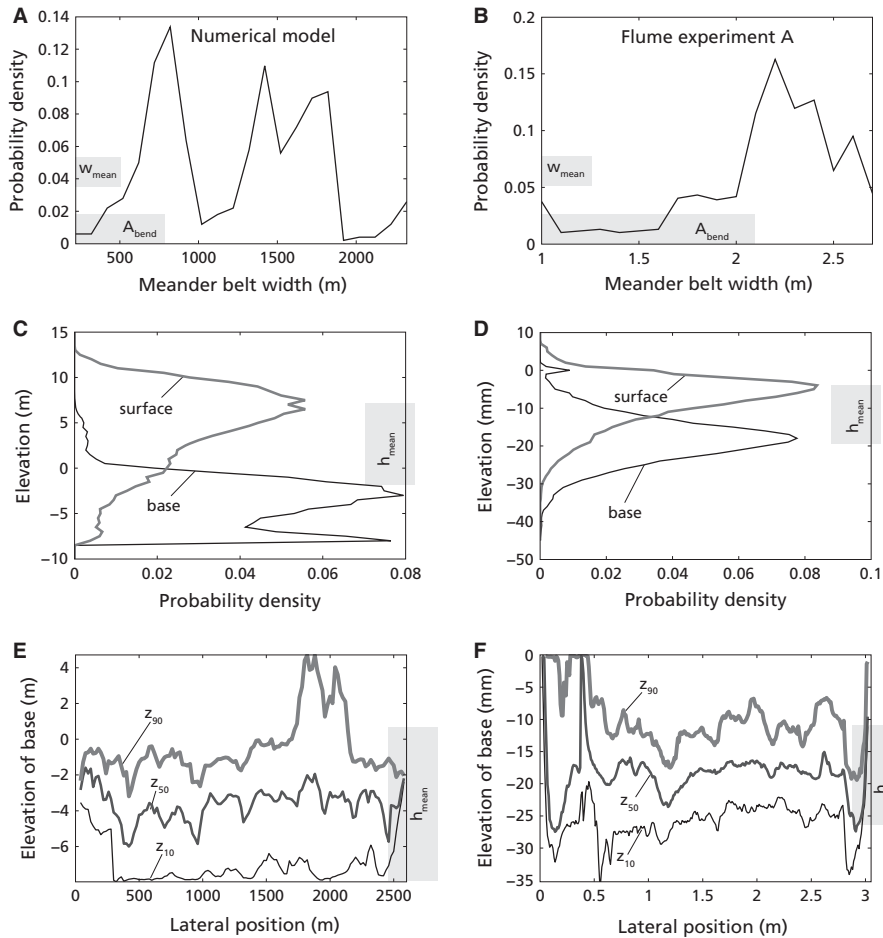


Fig. 6. Quantification of the external geometry of the meander belt sandbody. Probability density distributions of the width of the sandbody in (A) the numerical model and (B) flume experiment A. Probability density distributions of the relief in elevation at the surface (i.e. topography) and at the base of the meander belt sandbody in (C) the numerical model and (D) flume experiment A. Percentiles of the base relief as a function of the lateral position within the meander belt in (E) the numerical model and (F) flume experiment A.

sandbody, most evident from the Z_{50} percentile profile (Fig. 6F). Nevertheless, the downstream half of the left-hand margin of the sandbody base was much shallower, as indicated by the Z_{90} percentile profile. The relief in elevation of the base of the sandbody was generally captured by h_{mean} for the numerical model as well as flume experiment A (Fig. 6E and F). Base relief was primarily caused by in-channel depth variations. Persistence of the meandering channel to remain in the same location, deep outer bends, cut-off channels and confluence scours all resulted in a deepening of the base of the sandbody. In the numerical model, the relief was homogeneous and the base shallowed towards the margins while in flume experiment A the relief of the base was more irregular and a deepening of the base towards the margins of the sandbody was present. These different base expressions may either be the result of the different styles of meandering in flume experiment A and the numerical model, or an artefact of the numerical model's limitations in representing the deepest channel scours.

In flume experiment A, the base relief of the sandbody was similar to the topographical relief at the surface of the sandbody (Fig. 6D). In the numerical model, the deepest channel scours were not well reproduced (Fig. 6C). Consequently, the relief in elevation at the base of the sandbody was smaller than the topographical relief.

Combining the width and thickness statistics into dimensionless sandbody geometrical ratios resulted in similar outcomes for flume experiment A and the numerical model (Fig. 7A). Flume experiment A had a sandbody width-to-thickness ratio of 175 and the numerical model had a ratio of 150 at the end of the simulation. In flume experiment A, however, the spread in thickness around the average sandbody thickness of the belt was larger than in the numerical model (Fig. 7A). In flume experiment A, sandbody thicknesses of up to 4.5 cm (*ca* $3 h_{mean}$) were observed while the maximum sandbody thickness in the numerical model was 20 m (*ca* $2.5 h_{mean}$). In contrast, the spread in sandbody width was larger in the numerical model than in experiment A (Fig. 7A). In the numerical model, the width of the sandbody varied between 500 m (*ca* $2 w_{mean}$) and 2000 m (*ca* $8 w_{mean}$) while in flume experiment A the sandbody width was more uniform and ranged between 2 m (*ca* $8 w_{mean}$) and 2.5 m (*ca* $10 w_{mean}$).

Internal sandbody architecture

The dimensions of the meandering channel (depth, meander length, meander amplitude) as well as the succession of migrating and scouring channels determined the formation and preservation of bounding surfaces and contacts within the sandbody. Vertically, the deepest channels

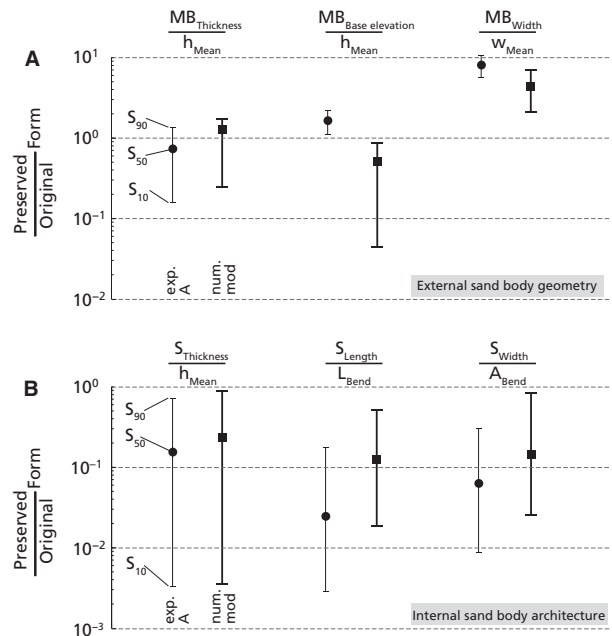


Fig. 7. Relation between preserved truncated and original non-truncated channel form. (A) Characterization of the external sandbody geometry of a meander belt (MB) by percentiles of the ratio between $MB_{thickness}$ and h_{mean} , between $MB_{base\ elevation}$ and h_{mean} , and between MB_{width} and w_{mean} . (B) Characterization of the internal sandbody architecture of a meander belt by percentiles of the ratio between $S_{thickness}$ and h_{mean} between S_{length} and L_{bend} and between S_{width} and A_{bend} .

left behind the thickest channel and bar deposits. These were then reworked and dissected and decreased in thickness by shallower channels as the flume experiment and numerical simulation progressed (Fig. 3). Horizontally, the meander bends with the largest length and amplitude formed the longest and widest deposits, which were eventually cross-cut and reworked by cut-offs at a later stage. This conceptual framework highlights that the succession of the meandering channels migrating across the fluvial landscape ultimately determined where the internal sandbody architecture consisted of thick, long and wide deposits and also where these deposits were reworked and therefore thinned, shortened and narrowed again.

Deposits were generally more fragmented in flume experiment A than in the numerical model (Fig. 8B). Experiment A produced a more mature channel belt in the sense that more cut-offs were recorded that reworked previously deposited bar deposits. In the numerical model, the deposits were on average 77% shorter, 67% narrower and 61% thinner than the original (L_{bend} , A_{bend} and h_{mean}) morphological form. In flume experiment A, the deposits were on average 87% shorter, 88% narrower and 71% thinner than the original morphological form. Reworking cross-cuts older deposits and thus thins,

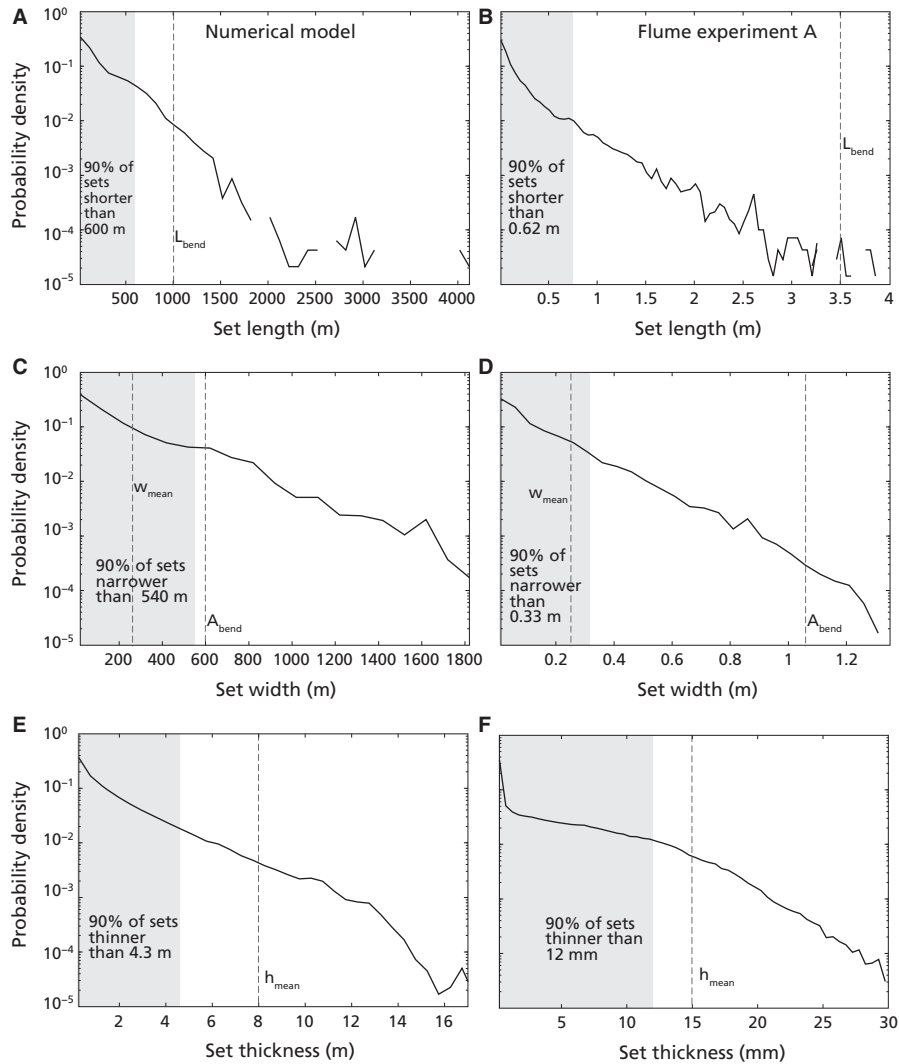


Fig. 8. Descriptive statistics of the internal sandbody architecture of meander belts. Probability density distributions of set length for (A) the numerical model and (B) flume experiment A. Probability density distributions of set width for (C) the numerical model and (D) flume experiment A. Probability density distributions of set thickness for (E) the numerical model and (F) flume experiment A. Note that most of the internal sandbody architecture is fragmented and notably shorter, narrower and thinner than the original (L_{bend} , A_{bend} and h_{mean}) channel form.

shortens and narrows them. The number of stacked sets in a vertical virtual core was used as a measure to quantify and compare the degree of reworking in flume experiment A and in the numerical model. In flume experiment A, we observed an average of 2.61 stacked sets per core and in the numerical model an average of 1.86 stacked sets per core. This indicates that the deposits in the numerical model were less frequently reworked, which explains the overall lower degree of fragmentation of the internal sandbody architecture in all three dimensions.

The higher degree of fragmentation in flume experiment A was also seen in the dimensionless ratios between set length, set width and set thickness. In the numerical model, the set length-to-width ratio was 1.2, the set

width-to-thickness ratio was 64 and the set length-to-thickness ratio was 74. In flume experiment A, the set length-to-width ratio was 1.1, the set width-to-thickness ratio was 30 and the set length-to-thickness ratio was 33. This shows that sets were notably narrower and shorter relative to their thickness in flume experiment A compared to the numerical model, which can have been due to the larger number of bend cut-offs recorded in flume experiment A.

Systematic lateral differences in scouring of the meandering channel and resultant reworking of older point bar deposits were observed in flume experiment A as well as the numerical model. In flume experiment A and in the numerical model, most of the morphological activity (i.e.

point bar formation and cut-offs) took place in a narrow zone surrounding the meander belt axis (Fig. 9). For example, four major cut-offs were observed in flume experiment A and the numerical model which took place within a corridor corresponding to 50% and 20% of the meander belt width, respectively. In this axial zone of the meander belt, point bar deposits that were formed early in the experiment and numerical simulation were likely reworked and cross-cut later. Closer to the margins of the meander belt, point bar deposits were less frequently and less substantially reworked.

Logically, the lateral differences in scouring and reworking frequency of the meandering channel resulted in lateral differences within the sandbody architecture (Fig. 10). For an arbitrary division into a central (i.e. middle third of total width) and marginal zone (i.e. summation of outer thirds of total width) of the meander belt width (Table 2), the sets were about 20% and 30% thinner in the central zone compared to the marginal zone in experiment A and the numerical model, respectively. In contrast to set thickness, no clear lateral trends in width and length of the sets were observed for flume experiment A and the numerical model (Table 2). The set distributions showed a tendency towards longer sets for the marginal zones in the numerical model (Fig. 10A) while instead shorter sets were more likely to be present in the marginal zones in flume experiment A (Fig. 10B). For both the numerical model and flume experiment A, the set distributions showed a tendency towards wider sets in the central zone of the meander belt although the differences between axial and marginal zones were small (Fig. 10C and D).

The style of channel cut-offs had a large impact on set width. In the chute-cut-off-dominated flume experiment

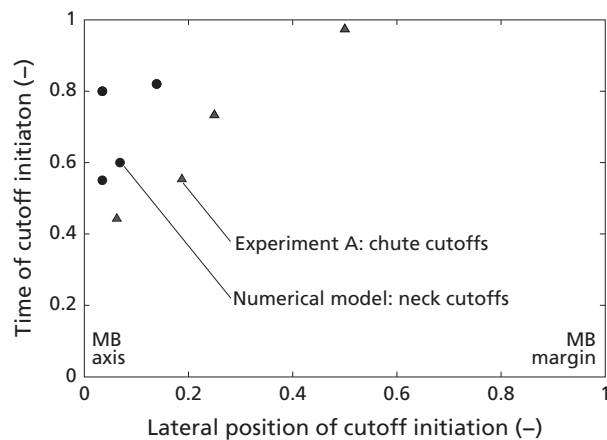


Fig. 9. Lateral position of channel cut-off initiation within the meander belt sand bodies formed in flume experiment A and the numerical model.

A, sets were on average 88% narrower than the original meander bend amplitude. In the neck-cut-off-dominated numerical model, sets were on average 67% narrower than the original meander bend amplitude. The reason for this difference in sandbody architecture was that the neck cut-offs in the numerical model occurred in a narrow zone (<20% of the meander belt width) close to the meander belt axis (Fig. 9). In contrast, the chute cut-offs in flume experiment A took place in a much wider zone, much farther from the meander belt axis. Consequently, reworking in the numerical model took place in a narrow axial zone over and over again, leaving marginal deposits relatively undisturbed while in flume experiment A even the margins of the sandbody were reworked, resulting in more, but on average narrower, sets across the sandbody in the lateral direction.

Lateral-accretion elements

Flume experiment B showed a variety of processes that controlled the distribution and dimension of fines within point bar deposits. In experiment B, the fine silt-sized silica flour was dominantly deposited in the upstream half of the experimental reach (Fig. 11). This indicates that most of the silt behaved as bedload and that only the finest fraction was able to spill overbank. In these overbank areas, flow velocities rapidly decreased. The fine silt that spilled overbank was therefore generally deposited close to the main channel forming small levees and splays.

Silt was also deposited at the point bar surface for which two depositional mechanisms were observed (Figs 11 and 12A). The first mechanism proceeded from water spilling onto the point bar surface thus depositing a silt drape on the point bar surface. This occurred throughout the experiment but intensified as the meander bend sharpened during the later phases of the experiment. The second mechanism was related to the variable discharge used in this experiment. During the high-flow stages, sediment was often eroded upstream of the point bar and was deposited again along the point bar forming a new scroll bar. During the low-flow stages, flow velocities generally decreased but the fine silt was still mobile and could settle on this newly formed scroll bar.

A more detailed analysis of fine silt deposition at the point bar surface (Fig. 12A) shows that the fines were mainly deposited at the point bar head (Fig. 12B) and in topographically lower point bar swales (Fig. 12C). During initial bar formation, high-flow velocities limited the settling of the fine-grained silt on the bar. Lateral accretion increased the bar amplitude, which raised water levels above bankfull level and resulted in overbank flow onto the point bar head, which explains the increase in silt in these regions. Since flow velocities were low on the point

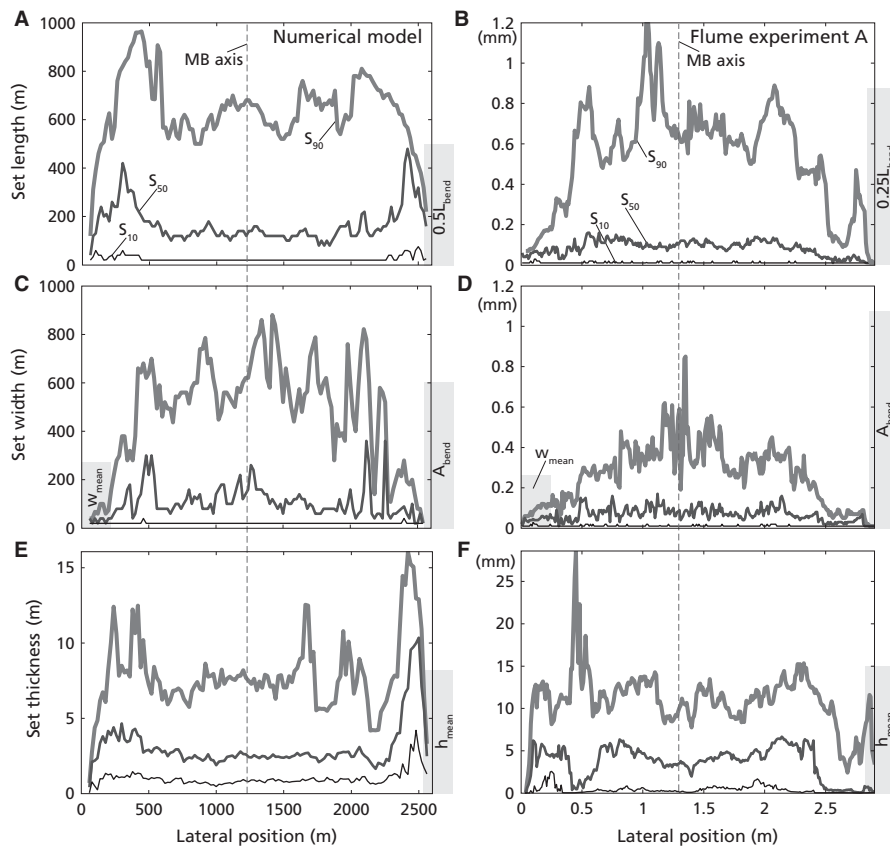


Fig. 10. Lateral differences in the internal sandbody architecture of meander belts. Percentiles of set length as a function of the lateral position within the meander belt for (A) the numerical model and (B) flume experiment A. Percentiles of set width as a function of the lateral position within the meander belt for (C) the numerical model and (D) flume experiment A. Percentiles of set thickness as a function of the lateral position within the meander belt for (E) the numerical model and (F) flume experiment A.

Table 2. Lateral differences in internal sandbody architecture of meander belts. The meander belt was arbitrarily divided into three equally wide zones with the middle zone defined as the centre of the meander belt. The set statistics of the two outer zones were averaged and here defined as the margin of the meander belt. Set thickness was normalized by h_{mean} , set length by L_{bend} and set width by A_{bend}

	Numerical model		Flume experiment A	
	Margin	Centre	Margin	Centre
Set thickness	0.44	0.31	0.30	0.25
Set length	0.21	0.20	0.09	0.08
Set width	0.23	0.26	0.11	0.13

bar surface, fines were predominantly deposited forming a thin silt sheet at this head area (Fig. 12B). Interestingly, the silt did not spread uniformly across the point bar surface (Fig. 12C). Five individual silt deposition peaks were identified, of which those at around 25 cm and 40 cm from the origin were related to increased silt deposition at the point bar head. The other three peaks were part of

a gradual rise in silt deposition from 60 cm onwards due to point bar lateral extension and meander bend sharpening. The three peaks in silt intensity as shown in Fig. 12C corresponded to topographically lower swales in which the silt was predominantly deposited. The result of this silt intensity pattern was an alternating topographical and associated grain-size pattern: high ridges that consisted of coarse sediment and low swales that were partly filled with fine silt.

Notably, the alternating surface grain-size pattern with concentrated peaks of silt was also present in the subsurface point bar deposits (Fig. 13). In the synthetic (Fig. 13A) and real (Fig. 13B) sediment peels of the point bar deposit in flume experiment B, laterally inclined surfaces were recognized, parts of which had fine silt draped on them.

A number of trends in silt deposition within the point bar deposit were identified. First, the thickest silt deposits were found at the point bar surface in the low-lying swales. Tracking these silt deposits from top to bottom revealed that they gradually thinned down the point bar

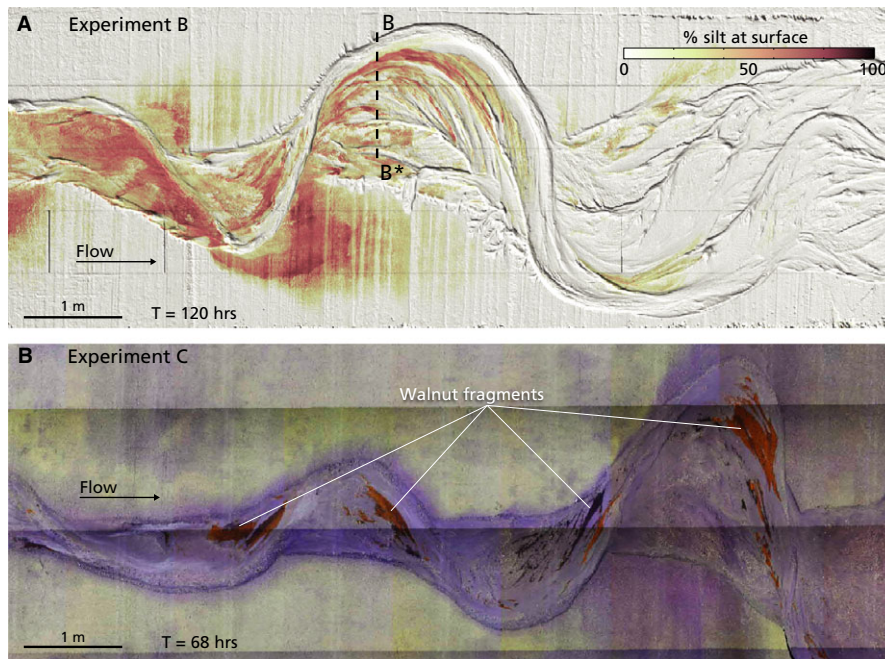


Fig. 11. Deposition of silt and walnut fragments. (A) Silt deposition in flume experiment B. Most of the silt is deposited in the upstream half of the experimental reach. Silt is predominantly deposited overbank forming splays, small levees and thin silt drapes on the point bar surface. Slice B-B* is presented in Fig. 13. (B) Deposition of walnut shell fragments in flume experiment C. Walnut shell fragments are mainly deposited in the downstream half of the point bar.

deposit along the lateral-accretion surfaces. The inclined silt drapes were mostly restricted to the upper 75% of the point bar deposit. Second, the outer point bar deposits, corresponding to later times of deposition (Fig. 13A), received more silt than the inner point bar. Third, silt was nearly absent in the downstream half of the point bar.

The slopes of the silt-draped lateral-accretion surfaces in flume experiment B corresponded well to the predicted transverse bed slope from Eq. 1 (Fig. 14). The slope of the lateral-accretion elements was typically about 5° . However, the variation between individual DEMs was considerable and the transverse bed slopes ranged from about 2° to 10° during the course of the experiment. Both the measured and predicted transverse bed slopes increased for a decreasing bend radius.

DISCUSSION

External geometry of meander belt sand bodies

The observed meander belt width-to-thickness ratios of experiment A and the numerical model are consistent with those reported for a range of ancient natural systems in Gibling (2006). The width-to-thickness ratios also

compare well with those reported for a variety of Holocene meander belts within the Rhine-Meuse delta and Lower Mississippi Valley (Gouw & Berendsen, 2007; Gouw & Autin, 2008). This indicates that a lower bound width-to-thickness ratio of 100 and an upper bound width-to-thickness ratio of 200 provide a robust estimate of the range of natural geometric variability of meander belt sand bodies.

Meander belt width-to-thickness ratios of 100 to 200 indicate wide and thin sand bodies. Importantly, this thin shape of meander belts suggests that most of the variation in sandbody geometry, facies and lithology is likely to be found laterally and not vertically. It is important to note that this is true for meander belt sand bodies formed in aggrading settings too. Although precise sedimentation conditions are unknown for the meander belts reported in Gibling (2006), it is likely that some of them were formed in aggrading settings. The much larger lateral than vertical extent of the meander belt sandbody, even for highly aggrading meander belts, was confirmed in a morphodynamic modelling study (Van de Lageweg *et al.*, 2015), which also related the volume of the sandbody to that of the floodplain in an effort to predict net-to-gross (i.e. the sand percentage) ratio.

A key result of this study is the quantification of the base relief of the meander belt sandbody. Similar to Best

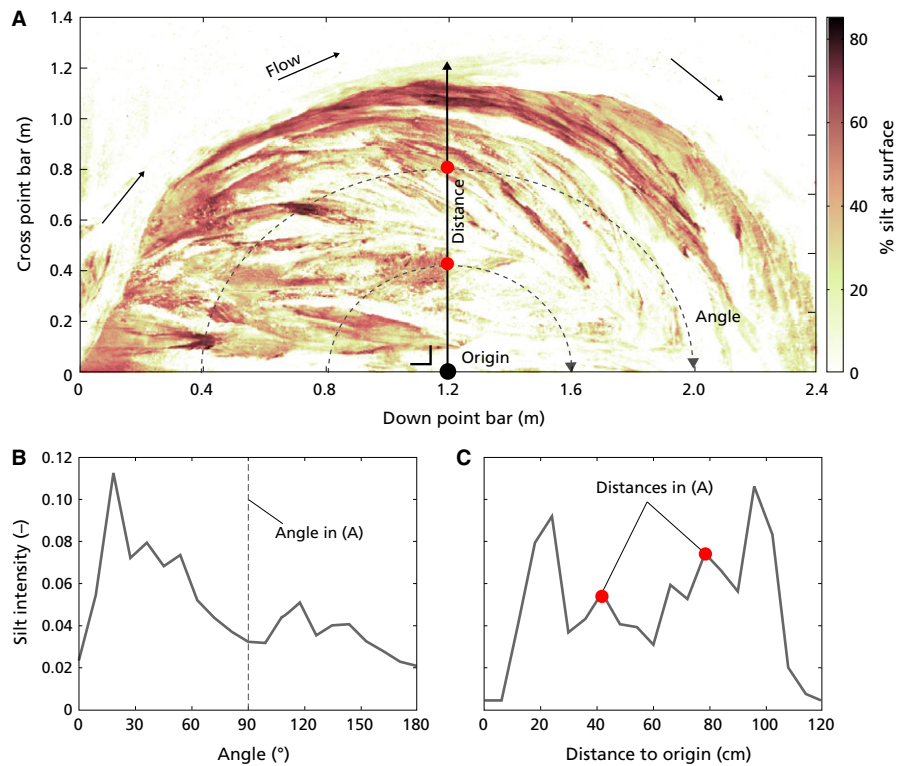


Fig. 12. Trends in silt intensity at the point bar surface that formed in flume experiment B. (A) Map view of silt concentration at point bar surface with definitions of origin, sector angle and distance. (B) Silt intensity as a function of the angle to the origin. (C) Silt intensity as a function of the distance to the origin. Silt concentrations are integrated for all analysed angles and distances to the origin and divided by the total silt concentration for all these points to calculate a silt intensity. Note that the silt intensity is high at the upstream side of the point bar and also increases with distance to the origin.

& Ashworth (1997) who reported on some channel junction scours in modern systems with 4–5 times greater incision than mean channel depth, a mean channel depth to deepest scour ratio of 3–5 was observed in this study. In turn, these topographical variations were reflected in the basal relief of the belts. Comprehensive characterization of the belt basal relief allows for better estimates of sand quantities, stacking patterns and connectedness of amalgamated meander belt sandstone bodies (Allen, 1978; Leeder, 1978; Bridge & Leeder, 1979; Bridge & Mackey, 1993; Bryant *et al.*, 1995; Heller & Paola, 1996; Ashworth *et al.*, 1999; Sheets *et al.*, 2002; Straub *et al.*, 2009; Hajek *et al.*, 2010). Well-exposed outcrops could theoretically be used to partially observe and quantify the relief at the base of natural ancient meandering systems (Holbrook, 2001) but this renders a far from complete three-dimensional image. Flume experiments and numerical models can help to reveal and map this hidden component of meander belt sand bodies and to that end, this study provides the first statistical distributions of the sandbody base relief.

In this study, two statistics were distilled that will be of use to characterize the base relief for natural meander belt systems. First, most of the base relief falls is captured

within h_{mean} since the majority of the topography is formed by features within and smaller than the main channel and deep scours are a relatively rare feature within the riverscape. An estimate of h_{mean} is therefore required to characterize the base relief of modern and ancient meander belts, which can perhaps be obtained from preserved channel fills at the margins of the meander belt. Second, flume experiment A showed that the probability density distributions of the meander belt topographical surface and sandbody base have a similar shape. This indicates that for modern meander belts an estimate of the base relief can be made based on the probability density of the meander belt topographical surface elevation. In turn, this also implies that modern analogues of ancient meander belts may provide some indication of the base relief of ancient systems.

Internal architecture of meander belt sand bodies

The internal architectures of the meander belt sand bodies generated in the numerical model and flume experiment A were quantitatively similar. Despite the differences in

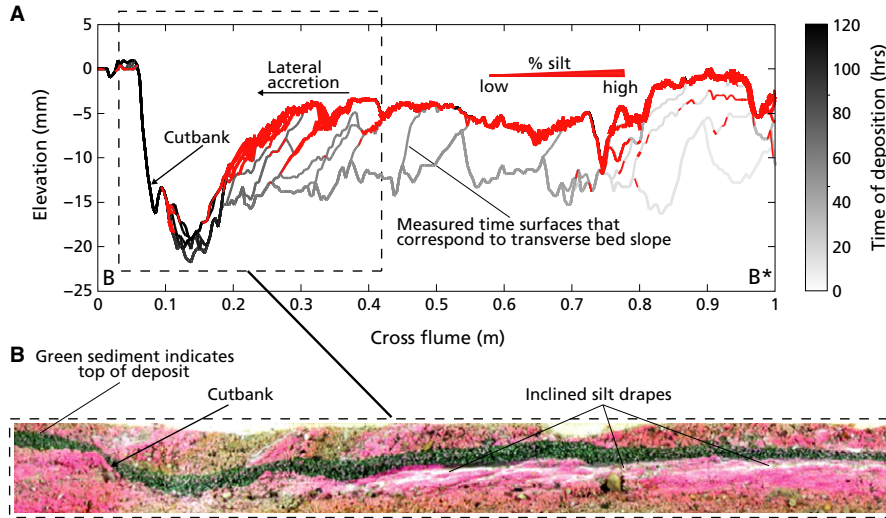


Fig. 13. Synthetic and real sediment peel of the point bar deposit in flume experiment B. The position of the slice B-B* is indicated in Fig. 11. (A) Synthetic slice of point bar deposit showing time of deposition and the amount of silt. Point bar deposits have lateral-accretion surfaces corresponding to the migrating transverse bed slope of the river channel. The measured time surfaces correspond to this transverse bed slope. (B) Sediment peel showing a detail of the point bar deposit in (A). This peel provides information on sedimentary structures and particle size trends. The silt-sized silica flour is white, the coloured green sediment indicates the top of the deposit and the pink colour is caused by the dye that was used to colour the water. Modified from Van de Lageweg *et al.* (2014).

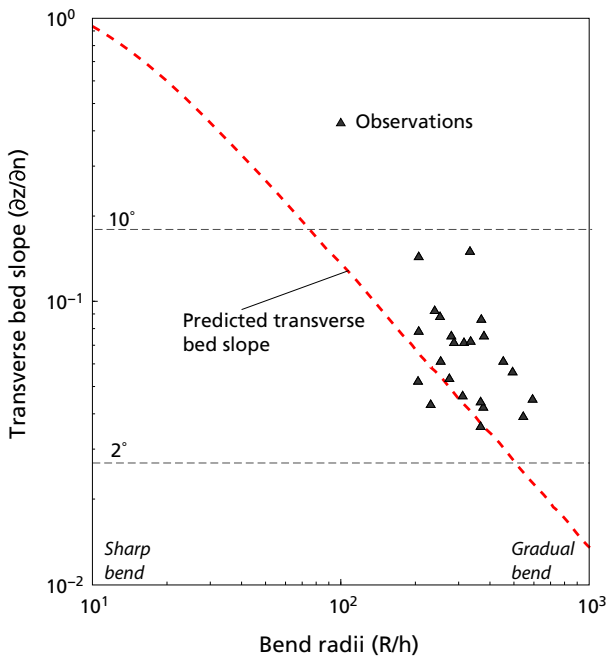


Fig. 14. Comparison of measured and predicted (Eq. 1) transverse bed slopes in flume experiment B. The transverse bed slope is measured at the meander bend apex for all time steps.

scale between the experimental and numerical rivers and resultant sand bodies, preservation ratios were consistent. For example, the ratio between the average preserved bar

deposit thickness and average depth of the meandering channel was 40% in the numerical model and 30% in flume experiment A. Such vertical (i.e. thickness) preservation ratios are consistent with those predicted for natural braided river systems (Paola & Borgman, 1991) but lower than those observed in the sandy braided South Saskatchewan River, Canada, pre-flood and post-flood (Parker *et al.*, 2013). Interestingly, similar vertical preservation ratios between the preserved deposit and original morphological form have been observed for a range of depositional environments. The ratio of mean cross-set thickness to mean dune height is 30% (Leclair, 2002; Jerolmack & Mohrig, 2005) and a similar preservation ratio exists for ripples (Storms *et al.*, 1999). This quantitative evidence highlights that in addition to meander belt sand bodies many other preserved architectures are also built up from truncated deposits, which are challenging to relate to the original non-truncated morphological form.

The ability to observe the formative processes is pivotal to understanding and explaining spatial differences in internal sandbody architectures between flume experiment A and the numerical model. The moderately sinuous chute-cut-off-dominated meandering river in flume experiment A and the highly sinuous neck-cut-off dominated meandering river in the numerical model both resulted in multiple, thin, stacked deposits in the axial zone of the sandbody with a gradual thickening of the deposits towards the margins of the sand bodies. Similar

lateral architectural trends have been reported for Quaternary meandering river systems (Lewin & Macklin, 2003), highlighting that fully preserved channel fills are most likely recovered close to the margins of a meander belt.

The difference in meandering style of chute cut-offs in flume experiment A and neck cut-offs in the numerical model affected the internal sandbody architectures. In this specific case of cut-off styles, the difference in architecture was most clearly seen in the width of the resultant deposits, with on average wider deposits produced by the neck-cut-off meandering system in which the cut-offs took place in a narrow zone. It is, however, likely that this specific case of chute-cut-off meandering style versus neck-cut-off meandering style can be extended to the majority of meandering processes leaving a specific imprint on the internal architecture of meander belt sand bodies, because the style of cut-off is a function of the degree of floodplain formation in freely meandering rivers (Kleinans & Van den Berg, 2011).

In addition to internal meandering dynamics, external conditions are also likely to impact the internal sandbody architecture of meander belts. For example, the degree of valley confinement is known to affect the style of meandering and thus the formation of the sandbody architecture. Ielpi & Ghinassi (2014) provide an example of how meandering style may affect sandbody architectures in their study on expansional and downstream-migrating point bar deposits in an exhumed Jurassic meander plain. They relate expansional point bars to meander belts in unconfined settings and find largely undisturbed deposits due to the limited reworking for this meandering style. In contrast, downstream-migrating point bars are often associated with a high degree of spatial confinement resulting in a high degree of reworking, low preservation of bar deposits, and a complex internal sandbody architecture (Alexander *et al.*, 1994; Ielpi & Ghinassi, 2014).

Lateral-accretion elements within point bar deposits

General grain-size trends derived from real and virtual sediment peels in flume experiment B are consistent with grain-size trends observed in natural coarse-grained point bar deposits (McGowen & Garner, 1970; Jackson, 1976; Bridge *et al.*, 1995). More important in the design of reservoir models, however, is a characterization of the dimensions and distributions of shales within point bar deposits. Primarily because the shales cause pronounced anisotropy in permeability (Novakovic *et al.*, 2002; Pranter *et al.*, 2007; Donselaar & Overeem, 2008; Willis & Tang, 2010), sometimes up to the point of unconnected chambers separated by barriers where disregarding the

shales would have led to the suggestion that the entire point bar is the container.

Flume experiments B and C showed a number of trends in the spatial distribution of fines that may help to refine depositional models of point bars (Figs 11 and 12). In flume experiment C, walnut shells were used instead of silt to simulate flow-limiting fines, while all other parameters were identical to those in experiment B. In both experiments, the fine-simulating sediments were predominantly deposited in the upper outer point bar deposits (Fig. 13). Inclined well-defined silt and walnut drapes were observed in the upper outer point bar bodies, which were interpreted to translate to inclined shales in natural point bars. The silt and walnut drapes were continuous in the upper half of the point bar, then became thinner and discontinuous when tracking them downward, with generally no fines present in the lower 25% of the point bar deposit. Importantly, these results from two different experiments independently indicate that shale drapes are most likely encountered in the upper outer point bar deposits, suggesting that in those areas anisotropy in permeability and compartmentalization may be largest.

Flume experiments B and C also differed in fine-sediment deposition in a number of ways (Fig. 11), highlighting our incomplete understanding of and limited ability to replicate these complex point bar deposits. First, the walnut fragments were predominantly deposited in the downstream half of the point bar, rather than the upstream half when using silt. The walnuts were deposited on the lee side of the point bar body where flow velocities were sufficiently decreased and the walnut fragments could settle. This shows that the difference in mobility between the walnut fragments and the silt had a large impact on the spatial distribution of fines within the point bar deposits. Second, walnut drapes were generally thicker and therefore laterally more continuous than the silt drapes. This may be a result of the specific material properties but the different behaviour hints at a potential relationship between fine-sediment properties and continuity of flow-limiting layers.

Dedicated flume experiments and numerical simulations are needed to further investigate relationship between fine-sediment properties and continuity of flow-limiting layers and to better characterize the spatial distribution and continuity of fines in point bar deposits. Walnut fragments and silt are only two means to represent fines in flume experiments and already show different depositional behaviour, potentially capturing different depositional behaviour in natural systems. The complexity of natural point bar deposits suggests that a combination of silt and walnuts and perhaps other materials is needed to comprehensively represent natural depositional behaviour and the spatial distribution and continuity of fines

in experimental point bar deposits. Combined with numerical simulations and detailed sedimentological studies across a range of natural point bars (McGowen & Garner, 1970; Jackson, 1976; Bridge *et al.*, 1995; Pranter *et al.*, 2007; Donselaar & Overeem, 2008), incorporating fine-grained and coarse-grained systems, this provides a powerful strategy to further improve our depositional models of these complex systems.

The dip of point bar lateral-accretion elements and the associated shale drapes is the second key parameter in the design of a reservoir model, in addition to the afore-discussed spatial distribution of shales. Flume experiment B provides quantification for this key parameter too. First, the dip of the point bar lateral-accretion elements in flume experiment B agrees well with theory (Eq. 1). Second, the dip of the silt drapes in flume experiment B is consistent with reported values for natural coarse-grained meandering systems (McGowen & Garner, 1970; Jackson, 1976; Bridge *et al.*, 1995). The dip of point bar lateral-accretion elements, that is the transverse bed slope, is a function of channel geometry and sediment composition. The large natural variation in these two parameters explains the large range of reported lateral-accretion dip slopes in natural point bars. Generally, sandy and sand-silt-mud rivers have a low width-to-depth ratio and can reach dip slopes up to 15° (Puigdefabregas & Van Vliet, 1978; Nanson, 1980; Mossop & Flach, 1983; Smith, 1987; Crerar & Arnott, 2007; Musial *et al.*, 2012). Gravelly and gravel-sand rivers typically have higher width-to-depth ratios resulting in lower (*ca* 5°) lateral-accretion dip slopes (McGowen & Garner, 1970; Jackson, 1976; Bridge *et al.*, 1995).

It is important to realize that the dip slope of potentially flow-limiting lateral-accretion elements of natural point bar deposits can be predicted from a few fairly basic morphological and sedimentological parameters (Table 3 and Fig. 15). This is illustrated for two modern and two ancient, and for two coarse-grained and two finer-grained meandering systems by making a comparison between the reported and predicted dip slopes. For this comparison, we selected the modern coarse-grained river Rhine, Germany (Erkens *et al.*, 2009), the modern finer-grained Daule river, Ecuador (Smith, 1987), the ancient coarse-grained Castisent Formation, Spain (Nijman & Puigdefabregas, 1978) and the ancient finer-grained McMurray Formation, Canada (Mossop & Flach, 1983; Crerar & Arnott, 2007; Musial *et al.*, 2012). Although a number of assumptions were made regarding h_{mean} for the ancient systems, the predicted dip slopes generally agreed well with the reported dip (Table 3) or observed dip by the authors (Fig. 15B). This demonstrates that robust predictions of the dip slopes of point bar lateral-accretion elements and the associated shale drapes can be made from readily available parameters.

Table 3. Application of transverse bed slope predictor (Eq. 1) to a number of modern and ancient fluvial meandering systems. Assumed for all systems was a valley slope of 10^{-5} m/m, a Chézy number of $25 \text{ m}^{0.5}/\text{s}$, a κ of 0.4 and a g of 9.81 m/s^2 . The first component of Eq. 1 ($9 \cdot (\frac{g}{h})^{0.3}$) is often calibrated and generally between 0.5 and 1.5 (Talmon *et al.*, 1995). A value of 1.0 was assumed for this component for all fluvial systems. Data for the river Rhine, Upper Rhine Graben (Germany) were derived from Erkens *et al.* (2009); for the Daule river (Ecuador) from Smith (1987); for the Eocene Castisent Formation (Spain) from Nijman & Puigdefabregas (1978); and for the Cretaceous McMurray Fm (Canada) from Mossop & Flach (1983), Crerar & Arnott (2007) and Musial *et al.* (2012)

Parameter	Rhine	Daule	Castisent	McMurray
h_{mean}	8 m	12 m	8 m	25 m
Sediment	Gravel to sand	Sand-silt-mud	Gravel to sand	Sand-silt-mud
Typical grain size	0.5 mm	0.125 mm	0.25 mm	0.125 mm
$\tan(\frac{\partial z}{\partial n})$	$0.37 \frac{g}{h}$	$0.15 \frac{g}{h}$	$0.26 \frac{g}{h}$	$0.11 \frac{g}{h}$
Typical $\frac{g}{h}$	125	40	100	40
Predicted dip	1–2°	8–9°	2°	13°
Observed dip	4–7°	12°	5°	8–12°

Application of archimetrics for reservoir characterization

The identified probability distributions on key archimetric parameters provide powerful new tools for geomodellers in characterizing reservoirs. Probability distributions allow geomodellers to obtain probabilities that reservoirs of certain dimensions or character may exist (Capen, 1992; Wood, 2004). This enables geomodellers to make quantitative judgements on the likelihood that their expert choices of sandbody dimensions and connectivity actually occur in the field – allowing for objective, probability-based, estimates of exploration success.

To assist geomodellers with making quantitative judgements on sandbody channel belt dimensions, probability density curves of the external geometry (Fig. 6) and internal architecture (Fig. 7) of meander belt sand bodies were constructed in this manuscript. Transforming these probability density curves into cumulative probability density curves allows for a probability-based assessment of the occurrence of sandbody dimensions. For example, the width of the meander belt sandbody generated with the numerical model has a P_{50} of 1320 m, with 80% of the sandbody width observations ranging between a P_{10} of 660 m and a P_{90} of 1820 m. Similarly, the thickness of the meander belt sandbody generated with the numerical model has a P_{50} of 6.4 m, with a less than 10% probability of finding a thickness greater than 9.7 m ($P_{90} = 9.7 \text{ m}$) or less than 1.9 m ($P_{10} = 1.9 \text{ m}$). Such simulated width and thickness dimensions are consistent

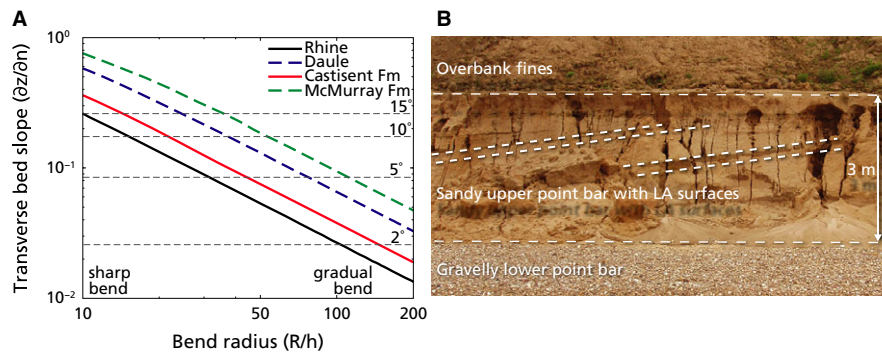


Fig. 15. Prediction of transverse bed slope for a number of modern and ancient fluvial meandering systems. (A) Transverse bed slope as a function of bend radius. (B) Section of a point bar deposit of the river Rhine in a quarry in Rheinberg, Germany (courtesy G. Erkens). The observed dip of the lateral-accretion surfaces varies between 4° and 7°, and is slightly higher than predicted from Eq. 1. The parameters used for the prediction of the transverse bed slopes are given in Table 3.

with the common ranges observed for natural preserved channel belt bodies of meandering rivers in the Holocene Rhine-Meuse delta (Gouw, 2008), the Holocene Lower Mississippi Valley (Aslan & Autin, 1999; Gouw & Berendsen, 2007; Gouw & Autin, 2008), and many other ancient fluvial meandering systems (Gibling, 2006; Rygel & Gibling, 2006). Notably, the width as well as the thickness of meander belt sand bodies are relatively easy to measure in outcrops and from three-dimensional seismic allowing knowledge of sandbody channel belt dimensions to be extrapolated from natural meandering systems to better inform geomodelling applications.

To generalize the findings of this study, normalized dimensionless sandbody dimensions and probability curves were derived for the flume experiment as well as the numerical model (Fig. 7). Dimensionless body dimensions and probability curves enable the results of this study to be used by geomodellers in characterizing reservoirs, if a number of key morphometrics such as typical channel depth and typical meander length of the target system are known. For example, the dimensionless ratio between the thickness of bar deposits and the depth of the meandering channel (i.e. the ratio between the preserved and original form) in the flume experiment has a P_{50} of 0.14, with 80% of the ratio observations ranging between a P_{10} of 0.003 and a P_{90} of 0.72. This means that for a natural target system with a typical channel depth of 10 m, 50% of the bar deposits would have a thickness of less than 1.4 m and 10% would have a thickness of more than 7.2 m, based on the probability curve derived from the flume experiment. Such a highly fragmented internal organization of meander belts is qualitatively substantiated by the identification of many architectural elements and hierarchy of bounding surfaces (Miall, 1985, 1988; Jordan & Pryor, 1992; Holbrook, 2001), emphasizing the heterogeneous nature of these deposits. Quantitative

support from natural systems for the highly fragmented internal organization of meander belts observed in this study arises from a study by Parker *et al.* (2013) in which repeated surface and subsurface surveys were used to establish how much of the barforms became truncated in response to a large flood. They found that unit bar deposits were truncated primarily in width (60%), in height (20%), and in length (32%) as compared with the formative bedform. With such a high degree of fragmentation of bar deposits in three dimensions following a single flood, the internal organization of a meander belt, which integrates the scouring and reworking effects of many floods, is likely to be composed of highly truncated deposits with fully preserved bar deposits and channel fills recorded although representing rare cases, as also quantified by the identified probability curves in this study (Fig. 7).

Archimetrics allow subsurface information to be combined with probability and statistics on reservoir dimensions and character, while taking reworking and partial preservation into account. Typically, a number of reservoir parameters (e.g. width and thickness of a sandstone body) are known in the development and production phases of meander belts serving as reservoirs. For the sake of simplicity and lacking information, geomodellers generally assume full preservation of geometrical body dimensions (e.g. point bar) derived from natural rivers to populate their geological models (Pranter *et al.*, 2007). Combining the reservoir parameters with the identified probability curves and statistics on reworked and partially preserved sandbody dimensions and character in this study provides a set of rules to refine the geological models. In particular, the probability curves provide geomodellers with a powerful quantitative tool to characterize a range of geometrical bodies and spatial trends in preservation of these bodies, in addition to the identified

information on the spatial distribution, dip angle, and continuity of flow-limiting shale drapes within point bar deposits. As a result, such refined geological models are anticipated to lead to more sophisticated lithology and porosity models, which ultimately cascades into better and more realistic flow simulations. The following scheme is proposed to maximize the applicability of the identified probability-based archimetrics:

1 Define the meander belt sandbody geometry (Fig. 1, sixth-order contacts). Two observables need to be estimated: average width and thickness of the sandbody. Typically, the width of the sandbody and its variation can be determined from seismic surveys. If not, the width should be estimated based on the thickness from well data and reported width-to-thickness ratios ranging from 100 to 200.

Well data are useful to quantify the meander belt thickness. This study indicates that most of the thickness variation is found laterally. Therefore, an effective strategy to quantify thickness variations, among other important stratigraphic and sedimentary parameters, is to drill wells along lateral transects.

A third parameter needed to quantify the sandbody geometry is the base relief. For the first time, this study provides a quantification of the base relief and shows that the relief is typically smaller than h_{mean} . h_{mean} can be estimated in two ways: from a fully preserved channel fill, which is most likely recovered close to the margins of a meander belt, or by estimating h_{mean} from the thickness of the meander belt sandbody. Observations in this study indicate that h_{mean} is equal to about one-third of the maximum sandbody thickness of the meander belt. This ratio was, however, obtained for a zero-net-depositional system and will be lower for net-depositional systems. Because the sedimentation conditions for most natural systems are unknown, the first approach to estimate h_{mean} is preferred.

2 Define the dimensions of the original meandering river. This is a crucial step because it allows one to connect the external geometry of the sandbody (Fig. 1, sixth-order contacts) to its internal architecture (Fig. 1, lower order contacts with a focus on third-order to fifth-order). Key morphometric parameters are h_{mean} , w_{mean} , L_{bend} and A_{bend} (Fig. 4). As stated in the previous step, h_{mean} is best estimated from a fully preserved channel fill. If such a channel fill is recovered, an estimate of w_{mean} can also be made. L_{bend} can be approximated in two ways. First, derive a typical L_{bend} from the undulating margins of meander belts for reservoirs with high-quality seismic data. Second, empirical relationships between L_{bend} and w_{mean} may be used for reservoirs with lower quality or no seismic data. Empirical relationships from modern rivers indicate that L_{bend}

is often equal to about 2.5–5 w_{mean} (Leopold & Wolman, 1957; Zeller, 1967). For easier field application, we approximated A_{bend} by 0.5 meander belt width. Dimensionless probability-based ratios between these key morphometric parameters and the identified archimetrics can now be used to further populate the reservoir (Fig. 7).

3 Use the archimetrics to build the internal sandbody architecture of meander belts (Fig. 1, third-order to fifth-order). As a first-order approximation of the dimensions of individual channel and bar architectural elements, a third of the original dimensions is reasonable. This indicates that a depositional body on average has a length of 0.3 L_{bend} , a width of 0.3 A_{bend} and a thickness of 0.3 h_{mean} .

Lateral architectural trends exist within the meander belt sandbody, with a general thickening of the deposits towards the margins of the meander belt. Therefore, further refinement of the internal sandbody architecture may be achieved by employing the entire dimensionless probability curves, although the number of available wells will determine the feasibility and confidence one can have in further refining the internal architecture. If a sufficient number of wells are available, it may be possible to estimate the degree of fragmentation from the number of stacked bar deposits. A higher number of stacked deposits is indicative of a higher degree of fragmentation, which logically results in shorter, narrower and thinner deposits.

4 Insert lateral-accretion surfaces within the individual channel and bar architectural elements. This implies that for every depositional body that is identified in the previous step an estimate of the presence, spatial distribution and dip of these surfaces needs to be made. Again, the number of wells defines to what level of detail this is possible. Currently, a robust and accurate depositional model predicting the spatial distribution of shale drapes acting as baffles or barriers to flow is lacking although our results suggest an increased likelihood of anisotropy and compartmentalization in upper outer point bar deposits, where shale drapes are best developed.

The dip angle and number of potentially flow-limiting lateral-accretion packages within point bar deposits can, however, be predicted robustly. A description of the parameters required to estimate the dip angle of the packages is given in Table 3. With this dip angle, the number of lateral-accretion packages within a point bar body can then be estimated from elementary geometrical considerations (Fig. 16). For example, for the McMurray Formation with a h_{mean} of 25 m, an average dip angle of about 10° and a typical R of 1000 m (Table 3), the average horizontal length of a lateral-accretion package is expected to be about 140 m. With a typical R of 1000 m, the point

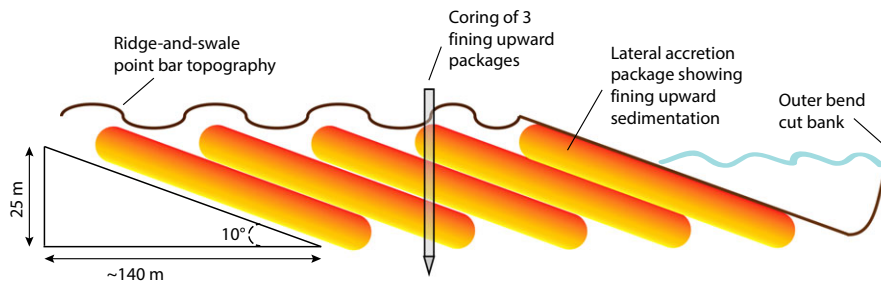


Fig. 16. Geometrical calculation of the number of potentially flow-limiting lateral-accretion packages within a point bar body. This example is based on the parameters derived for point bar deposits in the McMurray Formation with a typical channel depth of 25 m and a typical dip angle of the lateral-accretion packages of 10° (see Fig. 15 and Table 3). Based on these two parameters, a geometrical upper and lower bound prediction can be made on the number of flow-limiting packages a point bar body can host laterally and vertically. Note the vertical exaggeration of $2\times$.

bar body is expected to host a minimum of seven lateral-accretion packages and a maximum of about 15, depending on the degree of overlap applied between consecutive lateral-accretion packages. As a result of this lateral arrangement of the packages, two to four vertically stacked lateral-accretion packages are expected within this 25 m thick point bar body, where the number of vertically stacked packages depends on the position within the body and the lateral arrangement of the packages. These predictions are consistent with observations from photographs of point bar deposits of the McMurray Fm as seen in Musial *et al.* (2012, figures 8, 9 and 10) and supported by field observations made by author DB. Such straightforward geometrical considerations may therefore provide a simple and first-order estimate of the number of potentially flow-limiting lateral-accretion packages to be expected for a typical point bar in the field of interest, before gathering additional information to obtain a more detailed picture of the dimensions and distribution of these packages.

The presented archimetrics provide quantitative information on the external geometry and internal architecture of meander belt sand bodies. This is a first step towards a more quantitative understanding and characterization of meander belt sandbody architecture. A logical next step includes identification and characterization of truly three-dimensional architectural elements rather than providing probability curves for x , y and z independently. The latter approach lumps the architectural information on individual bodies such as channel fills and point bars into a single probability curve, while the former provides three-dimensional statistics describing individual architectural bodies. Also, Nicholas *et al.* (2016) present a simplified rule-based case to identify different populations associated with specific deposits such as dunes and unit bars within braided river deposits, though no attempt is made to quantify the different populations and their three-dimensional expression.

Object-based analysis (Deutsch & Tran, 2002; Novakovic *et al.*, 2002; Blaschke, 2010) can perhaps be extended to three dimensions to identify and discriminate between characteristics of channel fills, point bar sands, and point bar shales based on geometrical and sedimentary properties changing through time in experiments and models. Although computationally more demanding, this would provide for a more sophisticated analysis and a further refinement of the quantitative characterization of meander belt sandbody architecture feeding into reservoir models.

CONCLUSIONS

Three flume experiments and a numerical model were used to quantitatively describe the three-dimensional sandbody architecture of meander belts. The direct linkage between causal meander morphodynamics and resultant sandbody architecture allows the preserved and truncated deposits to be related to the original non-truncated meander form in three dimensions. The dimensionless results are general and applicable in detailed reservoir architecture studies. A hierarchical approach of bounding contacts was adopted to analyse and characterize the external geometry and internal sandbody architecture of meander belts, referred to as archimetrics. Results demonstrate that:

The external sandbody geometry of a meander belt is typically described by width-to-thickness ratios between 100 and 200. The relief at the base of meander belt sand bodies is smaller than h_{mean} . These ratios facilitate improved estimates of connectivity between amalgamated meander belt deposits.

The internal sandbody architecture consists of depositional bodies with on average a thickness of about 30% of the mean channel depth, 30% of the mean length of a meander and 30% of the mean amplitude of a meander. Although fully preserved channel fills and meander bends

are recovered, most of the internal architecture of meander belts consists of fragmented deposits.

The structure of the internal sandbody architecture is closely related to the meandering style. A general thickening of the deposits towards the margins of meander belts is seen although this trend is affected by processes such as, for example, neck-cut-off versus chute-cut-off and expansional-migrating versus downstream-migrating point bar style.

The transverse bed slope of the experimental lateral-accretion surfaces agrees well with a semi-empirical relationship. The application of this relationship with a number of natural modern and ancient meandering systems demonstrates that it predicts the slope and number of lateral-accretion packages within natural point bar deposits.

The identified probability distributions on key archimetric parameters provide powerful tools for geomodellers in characterizing reservoirs. A set of rules is outlined for building realistic three-dimensional reservoir models enabling geomodellers to make quantitative, probability-driven, judgements on the likelihood that their choices of sandbody dimensions occur in the field of interest.

ACKNOWLEDGEMENTS

We would like to thank two anonymous reviewers for comments that significantly improved the manuscript. WivdL was supported by ExxonMobil Upstream Research Company (grant EM01734 to MGK and G. Postma). MGK and WMvD were supported by the Netherlands Organisation for Scientific Research (NWO) (grant ALW-VIDI-864.08.007 to MGK). We are grateful to G. Erkens and K.M. Cohen for discussion. The authors contributed in the following proportions to conception and study design, data collection, analysis and conclusions, and manuscript preparation: WivdL (40, 60, 60, 90%), WMvD (10, 40, 10, 0%), DB (10, 0, 10, 0%), MGK (40, 0, 20, 10%).

References

- Alexander, J., Bridge, J.S., Leeder, M.R., Collier, R.E.L.L. and Gawthorpe, R.L. (1994) Holocene meanderbelt evolution in an active extensional basin, southwestern Montana. *J. Sed. Res.*, **64**, 542–559.
- Allen, J.R.L. (1978) Studies in fluvial sedimentation: an exploratory quantitative model for the architecture of avulsion-controlled alluvial suites. *Sed. Geol.*, **21**, 129–147.
- Asahi, K., Shimizu, Y., Nelson, J. and Parker, G. (2013) Numerical simulation of river meandering with self-evolving banks. *J. Geophys. Res. Earth Surf.*, **118**, 2208–2229. doi:10.1002/jgrf.20150.
- Ashworth, P.J., Best, J.L., Peakall, J. and Lorsche, J.A. (1999) Influence of aggradation rate on braided alluvial architecture: field study and physical scale-modelling of the Ashburton river gravels, Canterbury plains, New Zealand. In: *Fluvial Sedimentology VI* (Eds N.D. Smith and J. Rogers), pp. 333–346. Blackwell Publishing Ltd., Oxford, UK. doi: 10.1002/9781444304213.ch24.
- Aslan, A. and Autin, W.J. (1999) Evolution of the Holocene Mississippi River Floodplain, Ferriday, Louisiana: insights on the origin of fine-grained floodplains. *J. Sed. Res.*, **69**, 800–815.
- Best, J.L. and Ashworth, P.J. (1997) Scour in large braided rivers and the recognition of sequence stratigraphic boundaries. *Nature*, **387**, 275–277. doi:10.1038/387275a0.
- Bhattacharya, J.P. and Tye, R.S. (2004) Searching for modern Ferron analogs and application to subsurface interpretation. In: *Analog for Fluvial–Deltaic Reservoir Modeling: Ferron Sandstone of Utah* (Eds T.C. Chidsey Jr., R.D. Adams and T.H. Morrison), *Am. Assoc. Petrol. Geol. Stud. Geol.*, **50**, 39–58.
- Blaschke, T. (2010) Object based image analysis for remote sensing. *ISPRS J. Photogramm. Remote Sens.*, **65**, 2–16. doi:10.1016/j.isprsjprs.2009.06.004.
- Bridge, J.S. and Best, J.L. (1997) Preservation of planar laminae due to migration of low-relief bed waves over aggrading upper-stage plane beds: comparison of experimental data with theory. *Sedimentology*, **44**, 253–262. doi:10.1111/j.1365-3091.1997.tb01523.x.
- Bridge, J.S. and Leeder, M.R. (1979) A simulation model of alluvial stratigraphy. *Sedimentology*, **26**, 617–644.
- Bridge, J.S. and Mackey, S.D. (1993) A revised alluvial stratigraphy model. In: *Alluvial Sedimentation* (Eds M. Marzo, C. Puigdefabregas.), *Int. Assoc. Sed. Spec. Publ.*, **17**, 319–336.
- Bridge, J.S., Alexander, J., Collier, R.E.L., Gawthorpe, R.L. and Jarvis, J. (1995) Ground-penetrating radar and coring used to study the large-scale structure of point-bar deposits in three dimensions. *Sedimentology*, **42**, 839–852.
- Bryant, M., Falk, P. and Paola, C. (1995) Experimental study of avulsion frequency and rate of deposition. *Geology*, **23**, 365–368.
- Capen, E. (1992) *The Business of Petroleum Exploration*. AAPG Treatise of Petroleum Geology, Tulsa, United States, Dealing with Exploration Uncertainties, pp. 29–62.
- Crerar, E.E. and Arnott, R.W.C. (2007) Facies distribution and stratigraphic architecture of the Lower Cretaceous McMurray Formation, Lewis Property, northeastern Alberta. *Bull. Can. Pet. Geol.*, **55**, 99–124.
- Deutsch, C.V. and Tran, T.T. (2002) FLUVSIM: a program for object-based stochastic modeling of fluvial depositional systems. *Comput. Geosci.*, **28**, 525–535. doi:10.1016/S0098-3004(01)00075-9.
- Donselaar, M.E. and Overeem, I. (2008) Connectivity of fluvial point-bar deposits: an example from the Miocene

- Huesca fluvial fan, Ebro Basin, Spain. *AAPG Bull.*, **92**, 1109–1129. doi:10.1306/04180807079.
- Eke, E., Parker, G. and Shimizu, Y.** (2014) Numerical modeling of erosional and depositional bank processes in migrating river bends with self-formed width: morphodynamics of bar push and bank pull. *J. Geophys. Res. Earth Surf.*, **119**, 1455–1483. doi:10.1002/2013JF003020.
- Engelund, F. and Hansen, E.** (1967) *A Monograph on Sediment Transport in Alluvial Streams*. Teknisk Forlag, Kobenhavn, Denmark.
- Erkens, G., Dambeck, R., Volleberg, K.P., Bouman, M.T.I.J., Bos, J.A.A., Cohen, K.M., Wallinga, J. and Hoek, W.Z.** (2009) Fluvial terrace formation in the northern Upper Rhine Graben during the last 20000 years as a result of allogenic controls and autogenic evolution. *Geomorphology*, **103**, 476–495. doi:10.1016/j.geomorph.2008.07.021.
- Frascati, A. and Lanzoni, S.** (2013) A mathematical model for meandering rivers with varying width. *J. Geophys. Res. Earth Surf.*, **118**, 1641–1657. doi:10.1002/jgrf.20084.
- Gibling, M.R.** (2006) Width and thickness of fluvial channel bodies and valley fills in the geological record: a literature compilation and classification. *J. Sed. Res.*, **76**, 731–770. doi:10.2110/jsr.2006.060.
- Gouw, M.J.P.** (2008) Alluvial architecture of the Holocene Rhine-Meuse delta (The Netherlands). *Sedimentology*, **55**, 1487–1516. doi:10.1111/j.1365-3091.2008.00954.x.
- Gouw, M.J.P. and Autin, W.J.** (2008) Alluvial architecture of the Holocene Lower Mississippi Valley (U.S.A.) and a comparison with the Rhine-Meuse delta (The Netherlands). *Sed. Geol.*, **204**, 106–121. doi:10.1016/j.sedgeo.2008.01.003.
- Gouw, M.J. and Berendsen, H.J.A.** (2007) Variability of channel-belt dimensions and the consequences for alluvial architecture: observations from the Holocene Rhine-Meuse delta (The Netherlands) and Lower Mississippi Valley (USA). *J. Sed. Res.*, **77**, 124–138.
- Hajek, E.A., Heller, P.L. and Sheets, B.A.** (2010) Significance of channel-belt clustering in alluvial basins. *Geology*, **38**, 535–538. doi:10.1130/G30783.1.
- Heller, P.L. and Paola, C.** (1996) Downstream changes in alluvial architecture: an exploration of controls on channel-stacking patterns. *J. Sed. Res.*, **66**, 297–306.
- Holbrook, J.** (2001) Origin, genetic interrelationships, and stratigraphy over the continuum of fluvial channel-form bounding surfaces: an illustration from middle Cretaceous strata, southeastern Colorado. *Sed. Geol.*, **144**, 179–222.
- Ielpi, A. and Ghinassi, M.** (2014) Planform architecture, stratigraphic signature and morphodynamics of an exhumed Jurassic Meander plain Scalby Formation, Yorkshire, UK. *Sedimentology*, **61**, 1923–1960. doi:10.1111/sed.12122.
- Jackson, R.G.** (1976) Depositional model of point bars in the Wabash River. *J. Sed. Petrol.*, **46**, 579–594.
- Jerolmack, D.J. and Mohrig, D.** (2005) Frozen dynamics of migrating bedforms. *Geology*, **33**, 57–60.
- Jordan, D.W. and Pryor, W.A.** (1992) Hierarchical levels of heterogeneity in a Mississippi River Meander belt and application to reservoir systems. *AAPG Bull.*, **76**, 1601–1624.
- Kleinhans, M.G. and Van den Berg, J.H.** (2011) River channel and bar patterns explained and predicted by an empirical and a physics-based method. *Earth Surf. Proc. Land.*, **36**, 721–738. doi:10.1002/esp.2090.
- Kleinhans, M.G., van Dijk, W.M., van de Lageweg, W.I., Hoendervoogt, R., Markies, H. and Schuurman, F.** (2010) *From Nature to Lab: Scaling Self-Formed Meandering and Braided Rivers*. River.ow 2010, volume 2, edited by Dittrich, Koll, Aberle and Geisenhainer, pp. 1001–1010. Bundesanstalt für Wasserbau.
- Kleinhans, M.G., Haas, T.D., Lavooi, E. and Makaske, B.** (2012) Evaluating competing hypotheses for the origin and dynamics of river anastomosis. *Earth Surf. Proc. Land.*, **37**, 1337–1351. doi:10.1002/esp.3282.
- Kleinhans, M.G., van Dijk, W.M., van de Lageweg, W.I., Hoyal, D.C.J.D., Markies, H., van Maarseveen, M., Roosendaal, C., van Weesep, W., van Breemen, D., Hoendervoogt, R. and Cheshier, N.** (2014) Quantifiable effectiveness of experimental scaling of river- and delta morphodynamics and stratigraphy. *Earth-Sci. Rev.*, **133**, 43–61. doi:10.1016/j.earscirev.2014.03.001.
- Lanzoni, S. and Seminara, G.** (2006) On the nature of meander instability. *Water Resour. Res.*, **111**, F04006.
- Leclair, S.F.** (2002) Preservation of cross-strata due to the migration of subaqueous dunes: an experimental investigation. *Sedimentology*, **49**, 1157–1180.
- Leeder, M.** (1978) A quantitative stratigraphic model for alluvium, with special reference to channel deposit density and interconnectedness. In: *Fluvial Sedimentology* (Ed. A.D. Miall), *Bull. Can. Soc. Petrol. Geol. Mem.*, **5**, 587–596.
- Leopold, L.B. and Wolman, M.G.** (1957) River channel patterns: braided, meandering and straight. *U.S. Geol. Survey Prof. Paper*, **282-B**, 39–85.
- Lewin, J. and Macklin, M.G.** (2003) Preservation potential for Late Quaternary river alluvium. *J. Quatern. Sci.*, **18**, 107–120.
- Mackey, S.D. and Bridge, J.S.** (1995) Three-dimensional model of alluvial stratigraphy: theory and application. *J. Sed. Res.*, **B65**, 7–31.
- McGowen, J.H. and Garner, L.E.** (1970) Physiographic features and stratification types of coarse-grained point bars: modern and ancient examples. *Sedimentology*, **14**, 77–111.
- Miall, A.D.** (1985) Architectural-element analysis: a new method of facies analysis applied to fluvial deposits. *Earth Sci. Rev.*, **22**, 261–308.
- Miall, A.D.** (1988) Reservoir heterogeneities in fluvial sandstones: lessons from outcrop studies. *AAPG Bull.*, **72**, 682–697. doi:10.1306/703C8F01-1707-11D7-8645000102C1865D.

- Mossop, G.D. and Flach, P.D.** (1983) Deep channel sedimentation in the Lower Cretaceous McMurray Formation, Athabasca oil Sands, Alberta. *Sedimentology*, **30**, 493–509.
- Musial, G., Reynaud, J., Gingras, M.K., Fnis, H., Labourdette, R. and Parize, O.** (2012) Subsurface and outcrop characterization of large tidally influenced point bars of the Cretaceous McMurray Formation (Alberta, Canada). *Sed. Geol.*, **279**, 156–172. doi:10.1016/j.sedgeo.2011.04.020.
- Nanson, G.C.** (1980) Point bar and floodplain formation of the meandering Beatton River, northeastern British Columbia, Canada. *Sedimentology*, **27**, 3–29.
- Nicholas, A.P., Sambrook Smith, G.H., Amsler, M.L., Ashworth, P.J., Best, J.L., Hardy, R.J., Lane, S.N., Orfeo, O., Parsons, D.R., Reesink, A.J.H., Sandbach, S.D., Simpson, C.J. and Szupiany, R.N.** (2016) The role of discharge variability in determining alluvial stratigraphy. *Geology*, **44**, 3–6. doi:10.1130/G37215.1.
- Nijman, W. and Puigdefabregas, C.** (1978) *Fluvial Sedimentology*. Canadian Society of Petroleum Geologists Memoir, Coarse-Grained Point Bar Structure in a Molasse-Type Fluvial System, Eocene Castisent Sandstone Formation, South Pyrenean Basin, **5**, 487–510.
- Novakovic, D., White, C.D., Corbeanu, R.M., Hammon, W.S., III, Bhattacharya, J.P. and McMechan, G.A.** (2002) Hydraulic effects of shales in fluvial-deltaic deposits: ground-penetrating radar, outcrop observations, geostatistics, and three-dimensional flow modeling for the Ferron Sandstone, Utah. *Math. Geol.*, **34**, 857–893. doi:10.1023/A:1020980711937.
- Paola, C. and Borgman, L.** (1991) Reconstructing random topography from preserved stratification. *Sedimentology*, **38**, 553–565.
- Parker, N.O., Sambrook Smith, G.H., Ashworth, P.J., Best, J.L., Lane, S.N., Lunt, I.A., Simpson, C.J. and Thomas, R.E.** (2013) Quantification of the relation between surface morphodynamics and subsurface sedimentological product in sandy braided rivers. *Sedimentology*, **60**, 820–839. doi:10.1111/j.1365-3091.2012.01364.x.
- Peakall, J., Ashworth, P.J. and Best, J.L.** (2007) Meander-bend evolution, alluvial architecture, and the role of cohesion in sinuous river channels: a flume study. *J. Sed. Res.*, **77**, 197–212.
- Pranter, M.J., Ellison, A.I., Cole, R.D. and Patterson, P.E.** (2007) Analysis and modeling of intermediate-scale reservoir heterogeneity based on a fluvial point-bar outcrop analog, Williams Fork Formation, Piceance Basin, Colorado. *AAPG Bull.*, **91**, 1025–1051. doi:10.1306/02010706102.
- Puigdefabregas, C. and Van Vliet, A.** (1978) Meandering stream deposits from the Tertiary of the Southern Pyrenees. In: *Fluvial Sedimentology* (Ed. A.D. Miall), *Bull. Can. Soc. Petrol. Geol. Mem.*, **5**, 543–576.
- Rygel, M.C. and Gibling, M.R.** (2006) Natural geomorphic variability recorded in a high-accommodation setting: fluvial architecture of the Pennsylvanian Joggins Formation of Atlantic Canada. *J. Sed. Res.*, **76**, 1230–1251.
- Schuurman, F., Kleinhans, M.G. and Marra, W.A.** (2013) Physics-based modeling of large braided sand-bed rivers: bar pattern formation, dynamics, and sensitivity. *J. Geophys. Res. Earth Surf.*, **118**, 2509–2527. doi:10.1002/2013JF002896.
- Schuurman, F., Shimizu, Y., Iwasaki, T. and Kleinhans, M.** (2015) Dynamic perturbation in response to upstream perturbation and floodplain formation. *Geomorphology*, **253**, 94–109. doi:10.1016/j.geomorph.2015.05.039.
- Sheets, B.A., Hickson, T.A. and Paola, C.** (2002) Assembling the stratigraphic record: depositional patterns and time-scales in an experimental alluvial basin. *Basin Res.*, **14**, 287–301. doi:10.1046/j.1365-2117.2002.00185.x.
- Smith, D.G.** (1987) Recent developments in fluvial sedimentology. *Society of Economic Paleontologists and Mineralogists Special Publication*, Tulsa, Meandering River Point Bar Lithofacies Models: Modern and Ancient Examples Compared, **39**, 83–91.
- Storms, J.E.A., Dam, R.L.V. and Leclair, S.F.** (1999) Preservation of cross-sets due to migration of current ripples over aggrading and non-aggrading beds: comparison of experimental data with theory. *Sedimentology*, **46**, 189–200. doi:10.1046/j.1365-3091.1999.00212.x.
- Straub, K.M., Paola, C., Mohrig, D.C., Wolinsky, M.A. and George, T.** (2009) Compensational stacking of channelized sedimentary deposits. *J. Sed. Res.*, **79**, 673–688. doi:10.2110/jsr.2009.070.
- Struiksma, N.** (1985) Prediction of 2-D bed topography in rivers. *J. Hydraul. Eng.*, **111**, 1169–1182.
- Talmon, A.M., Struiksma, N. and van Mierlo, M.C.L.M.** (1995) Laboratory measurements of the direction of sediment transport on transverse alluvial-bed slopes. *J. Hydraul. Res.*, **33**, 495–517.
- Tyler, N. and Finley, R.** (1991) The three-dimensional facies architecture of terrigenous clastic sediments and its implications for hydrocarbon discovery and recovery. *SEPM Concepts in Sedimentology and Paleontology. Architectural Controls on the Recovery of Hydrocarbons from Sandstone Reservoir*, **3**, 1–5.
- Van de Lageweg, W.I., Van Dijk, W.M. and Kleinhans, M.G.** (2013a) Morphological and stratigraphical signature of floods in a braided gravel-bed river revealed from flume experiments. *J. Sed. Res.*, **83**, 1032–1045. doi:10.2110/jsr.2013.70.
- Van de Lageweg, W.I., Van Dijk, W.M. and Kleinhans, M.G.** (2013b) Channel belt architecture formed by a meandering river. *Sedimentology*, **60**, 840–859. doi:10.1111/j.1365-3091.2012.01365.x.
- Van de Lageweg, W.I., Van Dijk, W.M., Baar, A.W., Rutten, J. and Kleinhans, M.G.** (2014) Bank pull or bar push: what

- drives scroll-bar formation in meandering rivers? *Geology*, **42**, 319–322. doi:10.1130/G35192.1.
- Van de Lageweg, W.I., Schuurman, F., Cohen, K.M., Van Dijk, W.M., Shimizu, Y. and Kleinhans, M.G.** (2015) Preservation of meandering river channels in uniformly aggrading channel belts. *Sedimentology*, **63**, 586–608.
- Van Dijk, W.M., Van de Lageweg, W.I. and Kleinhans, M.G.** (2012) Experimental meandering river with chute cutoffs. *J. Geophys. Res. Earth Surf.*, **117**, F03023. doi:10.1029/2011JF002314.
- Van Dijk, W.M., Teske, R., Van de Lageweg, W.I. and Kleinhans, M.** (2013a) Effects of vegetation distribution on experimental river channel dynamics. *Water Resour. Res.*, **49**, 7558–7574. doi:10.1002/2013WR013574.
- Van Dijk, W.M., Van de Lageweg, W.I. and Kleinhans, M.** (2013b) Formation of a cohesive floodplain in a dynamic experimental meandering river. *Earth Surf. Proc. Land.*, **38**, 1550–1565. doi:10.1002/esp.3400.
- Van Rijn, L.C.** (1984) Sediment transport, part III: bed forms and alluvial roughness. *J. Hydraul. Eng.*, **110**, 1733–1754.
- White, C.D. and Barton, M.D.** (1999) Translating outcrop data to flow models, with applications to the Ferron sandstone. *SPEREE J.*, **2**, 341–350.
- Willis, B.J. and Tang, H.** (2010) Three-dimensional connectivity of point-bar deposits. *J. Sed. Res.*, **80**, 440–454.
- Willis, B.J. and White, C.D.** (2000) Quantitative outcrop data for flow simulation. *J. Sed. Res.*, **70**, 788–802.
- Wood, L.J.** (2004) Predicting tidal sand reservoir architecture using data from modern and ancient depositional systems. Integration of outcrop and modern analogs in reservoir modeling. *AAPG Mem.*, **80**, 45–66.
- Yang, C.S. and Sun, U.** (1988) Tide-influenced sedimentary environments and facies. In: *Tidal Sand Ridges on the East China Sea Shelf* (Ed. D. Boston), pp. 23–38. Reidel Publishing, Dordrecht.
- Zeller, J.** (1967) Meandering channels in Switzerland. *Int. Assoc. Sci. Hydrol. Publ.*, **75**, 174–186.
- Zolezzi, G., Luchi, R. and Tubino, M.** (2012) Modeling morphodynamic processes in meandering rivers with spatial width variations. *Rev. Geophys.*, **50**, RG4005. doi:10.1029/2012RG000392.